

# POLITECNICO DI TORINO

Master Thesis in Biomedical Engineering

Master Thesis

## **Impact of circular cross-section idealization in image-based computational hemodynamic models of coronary arteries.**



**Supervisor:** Dr. Diego Gallo

**Co-supervisor:** Prof. Umberto Morbiducci

**Master student**

Chiara Ferrero-Aprato

July 2019

# SUMMARY

ABSTRACT .....	3
1 INTRODUCTION.....	5
1.1 ANATOMY AND PHYSIOLOGY OF THE CARDIOVASCULAR SYSTEM.....	5
1.1.1 THE BLOOD COMPOSITION .....	9
1.2 THE BLOOD RHEOLOGY.....	11
1.3 FLUID DYNAMICS .....	16
1.4 CARDIOVASCULAR PATHOLOGIES.....	20
1.4.1 THROMBOSIS.....	21
1.4.2 ATHEROSCLEROSIS .....	22
1.4.3 SECONDARY PATHOLOGIES .....	26
2 ANALYSIS OF ATHEROSCLEROSIS.....	27
2.1 IMAGING TECHNIQUES.....	27
2.1.1 CORONARY ANGIOGRAPHY .....	27
2.1.2 INTRAVASCULAR ULTRASOUND .....	28
2.1.3 COMPUTED TOMOGRAPHY.....	28
2.1.4 OPTICAL COHERENCE TOMOGRAPHY .....	29
2.2 FUNCTIONAL CLINICAL ANALYSIS .....	29
2.2.1 FRACTIONAL FLOW RESERVE .....	29
2.2.2 INSTANTANEOUS WAVE-FREE RATIO (iFR) .....	31
2.2.3 CORONARY FLOW RESERVE (CFR).....	31
2.3 CFD ANALYSIS.....	33
2.3.1 GOVERNING EQUATIONS .....	34
2.3.2 TYPE OF BOUNDARY CONDITIONS .....	35
2.3.3 HAEMODYNAMIC DESCRIPTORS .....	38
3 MODELS CONSTRUCTION .....	43
3.1 IMAGES ACQUISITION .....	43
3.2 SEGMENTATION.....	43
3.2.1 VMTK SEGMENTATION .....	44
3.2.2 ITK-SNAP SEGMENTATION .....	44
3.2.3 MIMICS SEGMENTATION .....	45
3.3 FINAL MODELS CREATION.....	48

3.3.1 CIRCULAR SECTION AREA MODELS .....	49
3.3.2 MESH GENERATION.....	50
4 SIMULATIONS SETTING.....	53
4.1 THE FLOW EXTENSIONS .....	53
4.1.2 STEADY SIMULATIONS.....	54
4.2 MESH SENSITIVITY ANALYSIS .....	56
4.3 THE BOUNDARY CONDITIONS.....	59
4.3.1 THE INLET VELOCITY WEAVEFORMS .....	59
4.3.2 RESISTANCES SIZING.....	61
4.4 THE SETTING OF FINAL SIMULATIONS .....	62
5 RESULTS .....	64
5.1 SURFACE DESCRIPTORS ANALYSIS .....	64
5.1.1 TAWSS ANALYSIS.....	64
5.1.2 OSI ANALYSIS .....	66
5.1.3 RRT ANALYSIS .....	69
5.1.4 CORRESPONDANCES BETWEEN GEOMETRY DISTANCE AND SURFACE DESCRIPTORS DIFFERENCES .....	71
5.1.5 RISK-AREAS ANALYSIS .....	74
5.2 BULK-FLOW DESCRIPTORS ANALYSIS .....	78
6 CONCLUSIONS.....	82
BIBLIOGRAPHY .....	84

# ABSTRACT

Coronary artery diseases are one of the most common causes of death in developed countries, in particular atherosclerotic stenosis caused by formation of fibro adipose plaques or calcifications, that lead to a narrowing in vessel lumen. This reduction leads to a decrease in perfusion of downstream regions and could subsequently lead to ischemic phenomena and myocardial infarction.

Standard procedure for diagnosis of atherosclerotic lesions are invasive, but in recent years, image-based hemodynamic models obtained from computed tomography images combined with computational flow dynamics simulations is becoming a powerful tool, used to calculate descriptors useful to evaluate the fluid dynamic inside blood vessels and its effect on the atherogenesis.

To properly reconstruct a three-dimensional model, a tomographic acquisition of images is necessary, while in the case of planar acquisitions, like coronary angiography, using epipolar geometry is possible to obtain a three-dimensional reconstruction with the assumption of circular cross section of vessel.

The aim of this thesis is to understand the accuracy and the uncertainties associated to the assumption of circular cross-section, to do this, the same model was firstly reconstructed from computed tomography images provided by the *Dipartimento di Scienze Mediche, Divisione di Cardiologia, Azienda Ospedaliera Universitaria Città della Salute e della Scienza*, Turin, Italy, in particular left and right coronary arteries have been reconstructed. After that, using centrelines and radius information derived from the previous reconstructed models, the two models with circular cross section area have been obtained. To ensure grid independence and a lower computational cost, a mesh sensitivity study was performed. Prescribed boundary conditions were obtained from literature because in vivo measured data were not available for this patient.

Unsteady-state simulations were performed and hemodynamics were described in terms of both surface and bulk flow descriptors, in particular, near-wall hemodynamics was quantified in terms of wall shear stress-based descriptors, while bulk flow was described in terms of helical flow metrics, evaluating the differences between CT-models and circular section area models.

The goal of this study was to evaluate the approximation introduced by a reconstruction with circular cross-section area and its impact on the estimation of atheroprone areas. The results show that this approximation introduce a relevant underestimation of risk areas, this is surely dangerous because it can lead to neglect areas which are actually atheroprone, underestimating the atherogenic risk of the patient.

# 1 INTRODUCTION

## *1.1 ANATOMY AND PHYSIOLOGY OF THE CARDIOVASCULAR SYSTEM*

The cardiovascular system consists of: heart, the main organ that pumps blood, and a thick network of vessels through the whole body. The main functions of this system are performed by blood:

- Transporting of elements like oxygen, nutrients, byproducts of metabolism etc.
- Regulating of body temperature, fluid pH and the presence of the water in the cells;
- Organism defence;
- Reconstruction of damaged tissues.

The heart is divided into left heart and right heart and the two parts are separated by a thick septum. Each part is composed by an atrium and a ventricle connected by valves: the blood arrives in the atrium, passes through the ventricle and the latter pumps the blood in the circulation.

Vessels can be classified into two categories:

- Veins
- Arteries.

In general, the human cardiovascular system consists of several circuits connected to each other. The pulmonary circulation transports deoxygenated blood from the right heart to the lungs through the arteries; in the lungs the blood is oxygenated and is carried to the left heart by the veins.

Another circulatory loop system is the systemic circulation: the oxygenated blood flows from the left heart to tissues and organs through the arteries, in tissue capillaries the blood releases oxygen and nutrients and removes waste; finally, deoxygenated blood returns to right heart through the veins.

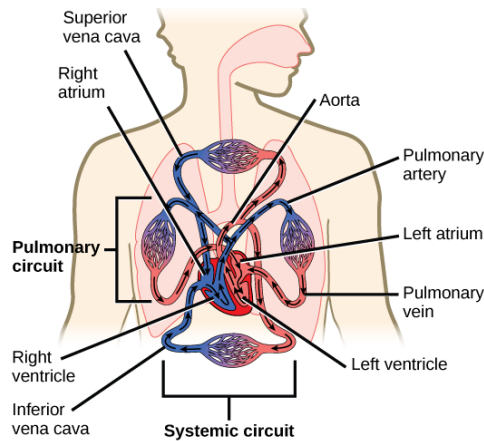


Figure 1.1 circulatory system [1]

Veins and arteries have the same histological structure: the wall has three layers and each of them is composed of a different kind of tissue.

The difference is the lumen calibre: arteries have smaller lumen but thicker walls than veins because they receive blood that flows with a higher pressure (Figure 1.2).

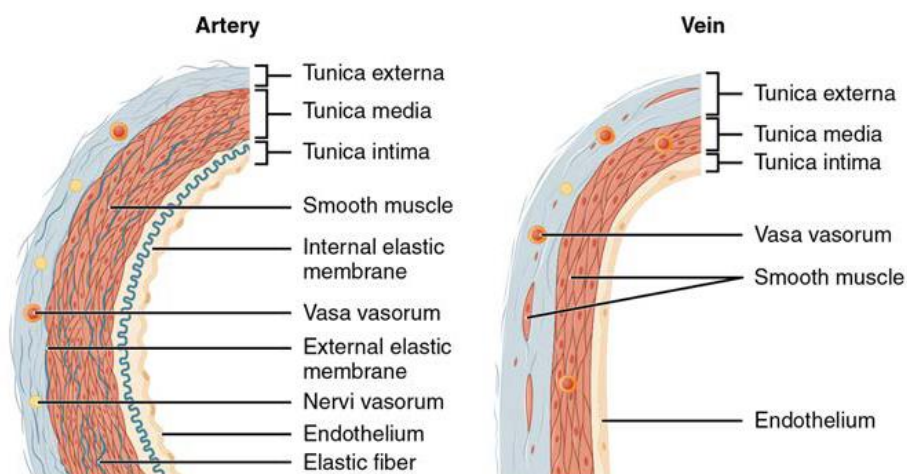


Figure 1.2 Structure of artery and vein wall [2]

The tunica intima is composed of a singular layer of endothelial cells in direct contact with blood and the basal lamina, a layer of connective tissue (collagen fibres) with important structural and filtering function. In the larger arteries, there is a thick discontinuous layer of elastic fibres called internal elastic lamina; there are small openings that have the purpose of exchanging materials between tunics.

The internal elastic lamina also has an important role for the structure of vessel: it allows the vessel to stretch during the cardiac cycle.

The tunica media is generally the thickest layer of vessel walls. It is the middle layer and its structure changes based on different vascular districts. It is composed of layers of smooth muscular tissue supported by elastic lamina and collagen fibres; the presence of muscles is important because their contraction or relaxation has an influence on the diameter of the lumen. Arteries, thanks to the high content of elastic fibres, have the role of regulating vasoconstriction and vasodilation; vasoconstriction decreases blood flow and increases blood pressure while vasodilation increases and decreases blood pressure; this behaviour is useful to cushion the pulsatile character of blood flow [3].

In larger arteries the external elastic lamina separates tunica media and tunica externa. The tunica externa (adventitia) is composed of connective tissue with collagen fibres, elastic fibres, some smooth muscle fibres, nerve connection and vasa vasorum (small vessels that carry nutrients and oxygen).

Arteries and veins can be further classified in order of magnitude:

- Artery circulatory system consists of elastic arteries, muscular arteries, arterioles and capillaries
- Vein circulatory system consists of large vein, medium size vein and venule.

Arteries carry blood from the heart to the peripheral tissue. Elastic arteries (diameter > 8 mm [2]) are essentially aorta and its branches, and their walls must be very elastic because during systole there is vasodilation as a consequence of increasing blood pressure and during diastole there is vasoconstriction; these arteries have the function of a second heart.

The tunica media is composed mainly of elastic fibres while the tunica externa is very thin and rich of collagen fibres, small vessels and nerves. Farther from the heart the percentage of elastic fibres in vessel walls decreases and the smooth muscle in tunica media increases.

In muscular arteries there is a smaller quantity of elastic fibres, therefore the vasodilation is limited; the tunica media is mainly composed of smooth muscular cells that play an important role in vasoconstriction that reduces the vessel lumen and increases flow resistance whenever a district needs less perfusion. There is no line of demarcation for the transition from elastic arteries and muscular, on the contrary, it is a gradual passage.



Arterioles (diameter between 20 and 100  $\mu\text{m}$ ) have the same three tunics, but with a different composition. Tunica media has one or two layers of smooth muscles and less elastic fibres, but the global thickness is very low. The small size of arteriole lumen causes a slowdown of the blood flow and the result is a decrease of pressure.

Capillaries are the smallest vessels in the circulatory system (calibre between 5-20 $\mu\text{m}$ ) and are composed of endothelium and basal lamina [2];

the wall is very thin to permit the exchange of materials. Capillary branches and venule branches form 3D networks, the so-called capillary beds.

The vessels mechanical properties depend on the mechanical properties of the vessel wall components. Each type of vessel has a different content of elastin, collagen and smooth muscle.

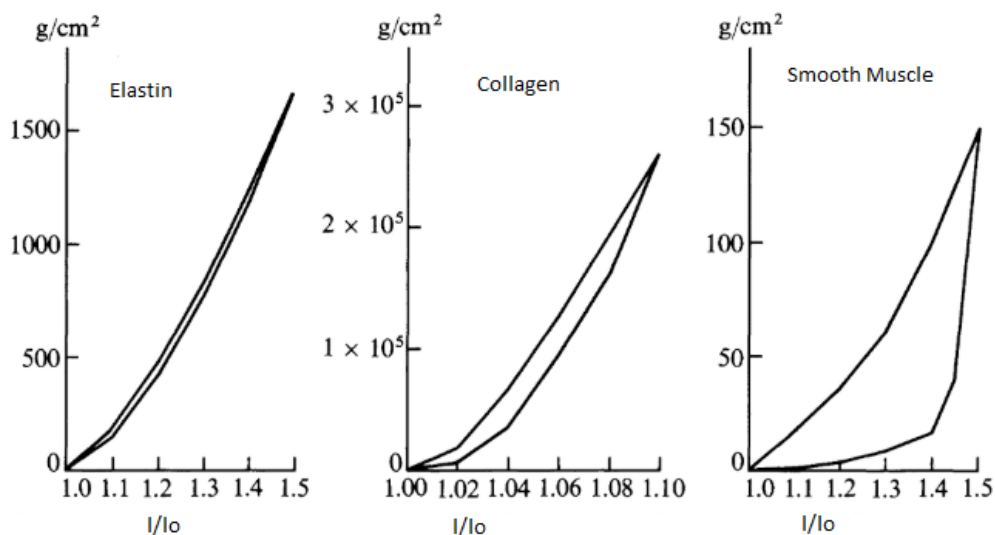


Figure 1.3 Mechanical response of the vessel wall materials to hysteresis loop stresses. Adapted from [3].

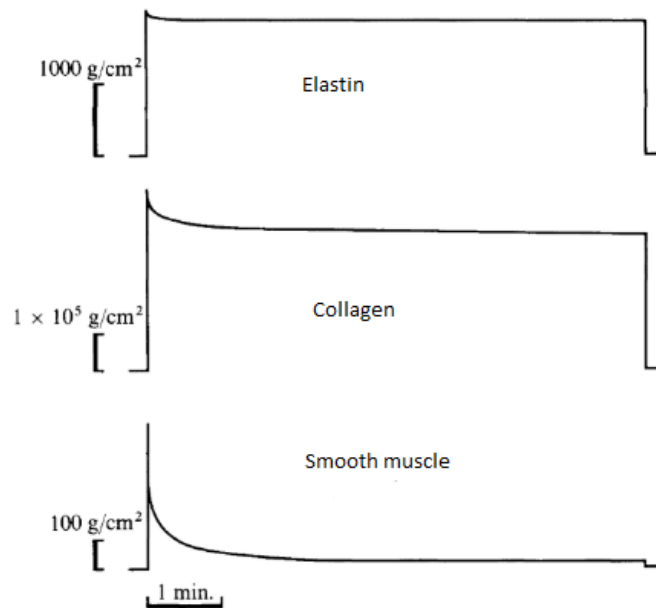


Figure 1.4 Mechanical response of the vessel wall materials to stress relaxation. Adapted from [3].

The elastin has low elastic modulus ( $E \approx \text{MPa}$ ) and its behaviour can be considered linear elastic as a first approximation; its level of relaxation and the hysteresis loop are very low. The collagen has an elastic modulus three order of magnitude higher than elastin Young's modulus. Its behaviour is not linear because the fibres progressively begin their action; the relaxation level is moderate. For the smooth muscle it is possible to notice a high hysteresis loop and, if the time is adequately long, the relaxation tends towards zero.

### 1.1.1 THE BLOOD COMPOSITION

Blood is a tissue composed of a suspension of different cells in a water solution called plasma.

The percentage in volume of blood corpuscular component is the haematocrit (Ht); this value is about 38-52% in a healthy man while in a healthy woman is about 36-46% [4] but it may vary based on pathologies or the altitude of the place where a subject is living. Cellular components are red blood cells (erythrocytes), white blood cells (leukocytes) and platelets (thrombocytes); all these elements originate from a single undifferentiated progenitor cell called hemocytoblast.

The production of blood corpuscular components is haematopoiesis and it takes place in the marrow of the diaphysis of long bones during the first years of life, then, in adulthood, it takes place in the marrow of short and flat bones.

### *ERYTHROCYTES*

Red blood cells (RBCs) are small cells with no nucleus with a diameter of 8  $\mu\text{m}$ . The shape is a biconcave disk with a plump periphery and a very thin centre bordered by a membrane called stroma: this specific configuration provides a greater surface area for gas exchanges.

Haemoglobin in erythrocyte cytoplasm constitutes 90 % of proteins contained in red blood cells. Haemoglobin acts as a carrier of oxygen and carbon dioxide and bonds are reversible. Haemoglobin is composed of four proteins and four molecules with iron ions; each iron ion can bond to an oxygen molecule, therefore each molecule of haemoglobin can transport four oxygen molecules.

Erythrocytes are continuously produced by hemocytoblasts in the bone marrow and their lifespan is around 90-120 days; they are then destroyed by spleen and liver.

RBCs are uniformly distributed in blood vessels thanks to the negative charge on the surface, but when the flow velocity is low erythrocytes pile up and form a structure called rouleaux. These structures can cause problems in blood circulation [4].

### *LEUKOCYTES*

White blood cells are elements with a nucleus and a cytoskeleton, developed in the whole cell volume. The cytoskeleton makes them less deformable than RBCs; also the percentage of WBCs in the blood is lower than RBCs'. The shape of these elements is spheroidal and they have a normal cellular and nucleus structure. Spleen, bone marrow and lymph nodes produce leukocytes, which plays an important role in defending the organism from external agents such as bacteria, viruses etc.

White blood cells can be divided into three big categories: monocytes, granulocytes and lymphocytes.

Monocytes are the largest blood cells and they are macrophage precursors. The tasks of these cells are phagocytosis and secretion activity: they produce defensive substances such as the interferons.

Granulocytes are divided into three categories: neutrophils (phagocytosis of microbes), eosinophils (phagocytosis of complex antigen-antibodies) and basophils (secretion of anticoagulant substances).

Lymphocytes have the task to recognize and destroy antigens: they mark external agents in order for monocytes and granulocytes to phagocytise them. Lymphocytes can be divided in two categories: lymphocytes T and B with a similar structure but different and complementary functions [4].

### *THROMBOCYTES*

Platelets are spherical or oval corpuscles with a diameter of about  $3\mu\text{m}$  with no nucleus. They have a fundamental role in blood coagulation (haemostasis): when a vessel shreds, thrombocytes stick to the wall and secrete substances that cause the platelet aggregation and the activation of the coagulation process. Platelets also have the function to stop external substances and fight infections [4].

### *PLASMA*

Plasma is the liquid part of the blood (90% of water) in which there are other substances: 90% of them are organic ones (lipids, proteins, hormones etc.) while the remaining percentage is composed of mineral substances in ionic form.

Proteins mainly deal with transporting nourishment and removing byproducts of metabolism [4].

## **1.2 THE BLOOD RHEOLOGY**

Rheology is the discipline that studies fluids behaviour. The cardiovascular system consists of flexible and non-rigid conduits in which a non-Newtonian fluid flows under the intermittent activity of the pumping heart. The blood, due to its corpuscular nature, can not be considered a homogeneous fluid and it does not present a Newtonian behaviour. Therefore, the blood has a very complex rheological behaviour, caused by the interaction between its components. Globulins, proteins contained in plasma, have a great influence on blood rheology and fibrinogen plays a fundamental role in cell aggregation.

A fluid is characterized by density and the viscosity. The blood density has a close correlation with the haematocrit:

$$\rho_s = (1 - Ht)\rho_p + Ht \rho_{gr} \quad (1.1)$$

Where  $\rho_p$  is the plasma density and  $\rho_{gr}$  is the density of corpuscular components of blood.

For an adult subject with  $Ht=45\%$  the blood density is around  $1056 \text{ Kg/m}^3$ . [4]

Viscosity represents the fluid's inertial resistance to flow and is also defined as the ratio of shear stress to velocity gradient. For shear rates below  $100 \text{ s}^{-1}$  blood has a non-Newtonian behaviour due to the formation of rouleaux. In practical terms, for vessels with a diameter higher than 0.3 mm the assumption of Newtonian behaviour of blood is acceptable because the average diameter of erythrocytes is at least two orders of magnitude lower than the vessels' diameter.

On the other hand, this assumption results not correct in vessels with a diameter lower than 0.3 mm. A normal value of blood viscosity is about  $3 \cdot 10^{-3} - 4 \cdot 10^{-3} \text{ Pa}\cdot\text{s}$  (3-4 cP) [4].

Blood viscosity depends on the viscosity of plasma that is, under normal conditions, around 1.1-1.6 cP, but it is affected by temperature because of the prevalence of water in plasma.

The water viscosity is related to temperature as shown in equation 1.2.

$$\mu_w = \frac{\mu_0}{(1+0.0337 T+0.00022 T^2)} \quad (1.2)$$

$\mu_0$  is water viscosity at  $T=0^\circ\text{C}$  ( $\mu_0=1.808 \text{ cP}$ ).

The plasma viscosity is function of water viscosity and temperature following the equations 1.3.

$$\begin{aligned} \mu_p &= 1.8 \mu_w & T < 20^\circ\text{C} \\ \mu_p &= \mu_w (1.32 + 0.024 T) & T > 20^\circ\text{C} \end{aligned} \quad (1.3)$$

Proteins also influence the plasma viscosity: a higher concentration of proteins increases the viscosity. Albumin (40% of plasma protein content) is the protein that most influences plasma viscosity. The relation between protein concentration ( $c$ ) and  $\mu_p$  is expressed in equation 1.4.

$$\mu_p = \mu_w \frac{1}{1-k c} \quad (1.4)$$

Blood rheological properties are also influenced by RBCs, haematocrit and erythrocytes deformability.

The haematocrit is a dynamic value that may change according to pathologies or physiology. In 1906, Einstein developed the first analytical model to determinate the viscosity of a spherical particles suspension in a homogeneous fluid, but he did not consider different particle morphologies.

$$\mu_{\text{susp}} = \mu_{\text{fluid}} \frac{1}{1-2.5 c} \quad (1.5)$$

In 1922, Jeffery introduced a geometric factor ( $b$ ) in the formula.

$$\mu_{\text{susp}} = \mu_{\text{fluid}} \frac{1+c}{1-b c} \quad (1.6)$$

Einstein's and Jeffery's viscosity equations have both an intrinsic limit: for the first  $c < 0.4$  and for the second  $c < 1/b$ . In practical terms, in order to calculate the blood viscosity a simplification is used.

$$\mu_s = \mu_p (1 + 2.5 \text{ Hct}) \quad (1.7)$$

There is a further model formulated by Taylor that considers the presence of fluid inside particles.

$$\mu_s = \mu_p \left( 1 + 2.5 \frac{\mu_r/\mu_p + 0.4}{\mu_r/\mu_p + 1} c \right) \quad (1.8)$$

Erythrocytes are deformable cells, so, when subjected to high shear forces they tend to assume an elliptical shape with its major axis aligned in the motion direction decreasing the fluid viscosity. The RBCs, with low shear rate, tend to form aggregates which cause an increase of viscosity. This blood behaviour is summarized in Figure 1.5.

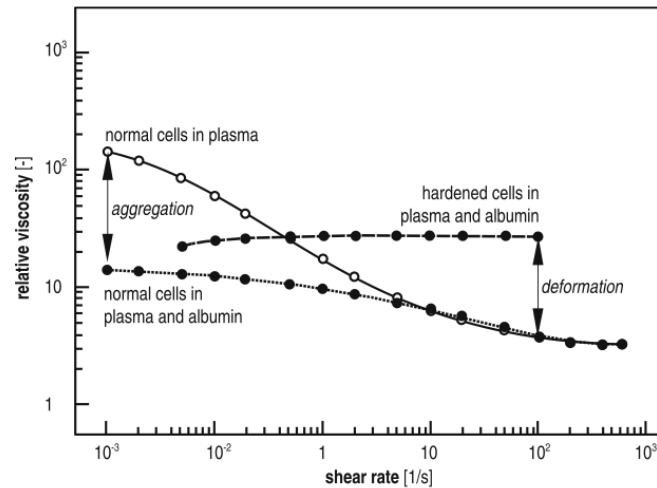


Figure 1.5 Relation between viscosity and shear rate for human blood [5]

The graphic shows the results of an experiment that compares the viscosity behaviour in three blood samples: one of normal blood, one of blood with hardened cells and the last with albumin enriched blood (cells can't aggregate).

### NON-NEWTONIAN MODELS

The bloodstream in the physiological system is a complex phenomenon and, when it is not possible to consider the blood a Newtonian fluid, it is necessary to introduce other models that better approximate the blood behaviour. A non-Newtonian fluid can be viscous (divided further into time-dependent and time-independent) or viscoelastic. The latter has a similar behaviour to a viscoelastic solid: it deforms, and it preserves a track of its history. Therefore, the dynamic viscosity is substituted by the apparent viscosity, that depends on the motion field used.

Various researcher created non-Newtonian models starting from experimental data, but in this work, we consider five of these models:

- *Bingham model*
- *Casson model*
- *Power-Law model*
- *Carreau model*

- *Generalised Power-Law model.*

The *Bingham model* is represented by the following relation

$$\tau = \tau_0 + \tau_B \dot{\gamma} \quad (1.9)$$

$\tau_0$  is the shear stress needed to move the fluid while  $\tau_B$  is Bingham's viscosity. This model is not a good approximation for blood shear rate lower than  $100 \text{ s}^{-1}$ , but it approaches asymptotic behaviour very closely.

In a Bingham fluid, the shear stress is directly proportioned to the conduit radius, therefore there is a value of radial coordinate ( $r_0$ ) to which it corresponds a shear stress value equal to  $\tau_0$ . The shear stress reaches its maximum at the wall.

The *Casson model* is described by the following relation

$$\sqrt{\tau} = \sqrt{\tau_0} + s \sqrt{\dot{\gamma}} \quad (1.10)$$

This formula has a similar significance to the previous one, but it was obtained by an interpolation of experimental data: experimental values derived from tests with blood samples at different values of haematocrit maintained at  $25^\circ\text{C}$ .

The *Power-Law model* is a blood viscosity model and the representative formula is as it follows

$$\mu(\dot{\gamma}) = k(\dot{\gamma})^{n-1} \quad (1.11)$$

$k$  is the flow consistence index and  $n$  is the Power-Law index; these indexes depend on haematocrit and on blood constituents [6]. *Walburn-Schneck* model is a simplification of Power-Law model but both models predict decreasing viscosity in regions with high shear rate and also in regions which should have a Newtonian fluid behaviour.

For this reason, *Cho and Kensey, 1991*, suggested that the Power-Law model could be modified using slightly different parameters; they also proposed that Power-Law model



could artificially mimic the Newtonian behaviour at shear rate values above  $226.5 \text{ s}^{-1}$  [7]. The main problem of this model is that it overestimates non-Newtonian effects. The *Generalized Power-Law* model was introduced by *Ballyk et al.* in 1994 and it is a general model for blood viscosity.

$$\mu(\dot{\gamma}) = \lambda(\dot{\gamma}) \dot{\gamma}^{n(\dot{\gamma})-1} \quad (1.12)$$

This model aims to solve the Power-Law model issue of overestimating non-Newtonian effects. It is a good approximation because, at low shear rate it approximates the Power-Law model while, at mid-high shear rate, it is close to the Newtonian model.

In the *Carreau model* the viscosity is given by

$$\mu(\dot{\gamma}) = \mu_{\infty} + (\mu_0 - \mu_{\infty})[1 + (\lambda\dot{\gamma})^a]^{(n-1)/a} \quad (1.13)$$

where  $a, n$  and  $\lambda$  are empirically determined parameters. The first two parameters are dimensionless and  $\lambda$  (s) is the relaxation factor; the latter represents the time it takes to pass from  $\mu_0$  to  $\mu_{\infty}$ . These two values are the viscosity limitation and  $\mu_{\infty}$  is the Newtonian fluid viscosity [7]. This model, for low values of shear rate ( $50 < \dot{\gamma} < 100 \text{ s}^{-1}$ ), underestimates the viscosity, so for shear rate lower than  $100 \text{ s}^{-1}$  Ballyk model is to be preferred. [8].

### 1.3 FLUID DYNAMICS

The functioning of blood circulation can be explained in terms of hydrodynamic laws and physical principles: according to the law of continuity, the flow through successive cross-section of a vessel, is constant.

If the flow is constant the speed variation is inverse to the cross-section area: when the area decreases the speed increases and vice versa. A reduction of vessel lumen (stenosis) causes an increment of speed and a reduction of distal segment perfusion. The speed increase and the alternation of accelerations and decelerations, caused by heart intermittency, induce the increment of kinetic energy.

There are two types of flow:

- Laminar flow characterized by highly ordered motion along coaxial cylindrical laminae; the velocity profile is parabolic when it is fully developed;
- Turbulent flow is a complex mechanism dominated by fluctuations and it is characterized by highly disordered motion.

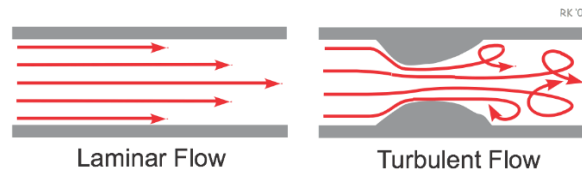


Figure 1.6 Difference between laminar and turbulent flow [9]

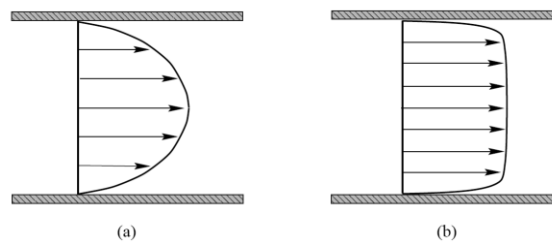


Figure 1.7 Velocity profiles: a) laminar b) turbulent [10]

The transition from laminar flow to turbulent flow is not very clear and depends on the diameter, the velocity and the character of the fluid (viscosity and density): there are regions where the flow randomly switches between laminar and turbulent.

Reynolds number ( $Re$ ) is a parameter used to evaluate the transition between the two types of flow; it represents the ratio between inertial forces and viscous forces [11].

$$Re = \frac{v_{avg} D \rho}{\mu} = \frac{\text{inertial forces}}{\text{viscous forces}} \quad (1.14)$$

Where  $v_{avg}$  is the mean velocity,  $D$  is the vessel diameter,  $\rho$  and  $\mu$  are respectively the density and the viscosity of the blood.

There is a critical value of  $Re$  that marks the transition from laminar to turbulent and it is  $Re=2300$  [11].

- $Re \leq 2300$  laminar flow;
- $2300 \leq Re \leq 4000$  transitional flow;
- $Re \geq 4000$  turbulent flow.

In absence of pathologies, the blood flow is considered turbulent only at the heart valves, but in presence of stenosis or plaques, the flow motion can be turbulent in the pathological vessels as well.

Giddens et al., in their study showed that the transition from laminar to turbulent flow depends on the area reduction of the stenosis and the critical Reynolds number changes along with different stenosis geometries and flow conditions; for instance, a more abrupt and sharpened stenosis causes a greater flow disturbance than a smooth configuration [12].

At coronaries level, studies showed that the flow may be considered laminar and Reynolds number is about 100 [13] [14].

The Hagen-Poiseuille law describes the flow of homogeneous and Newtonian fluid (one with a viscosity ( $\mu$ ) that doesn't change with velocity) through a cylindrical and rigid conduit of infinite length.

The Poiseuille law is based on the following assumptions:

- The fluid is Newtonian and homogeneous;
- The flow is steady, laminar and fully developed;
- The conduit wall is cylindrical and rigid;
- The no slip condition is valid.

This law is obtained with the integration of velocity of all concentric fluid rings scrolling and the multiplication by their areas.

$$Q = \frac{\pi \Delta P r^4}{8 \mu l} \quad (1.15)$$

$\Delta P$  is the pressure gradient,  $r$  and  $l$  are respectively the radius and the length of the conduit and  $\mu$  is the viscosity [11]. From this equation the resistance value  $R$  can be obtained, as the ratio between  $\Delta P$  and  $Q$ .

$$R = \frac{8 \eta l}{\pi r^4} \quad (1.16)$$

The vessel radius influences the resistance and consequently the flow. Arterioles, that have a diameter that is much lower than the arteries' calibre, are vessels that influence the most the resistance of the circulatory system [15].

The Hagen-Poiseuille law can be applied only for the boundary conditions in the cardiovascular system because of the vessels geometry and the blood characteristics.

Often, blood vessels present high curvatures; this conduit configuration produces a pressure gradient across the cross-section of the vessel. It is a consequence of the maximum axial velocity relocation in the direction of the outer part of the vessel wall curve [16]. The mechanism described is the secondary flow or Dean's flow [17]. Secondary flows are dissipative flow components and consist of pairs of counter-rotating vortices induced by the imbalance between pressure and centrifugal force.

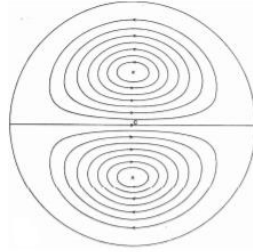


Figure 1.8 Dean vortices [18].

The Dean number is the ratio between centrifugal forces and viscous forces and appears in Dean-equations that are an approximation of Navier-Stokes equations.

$$Dn = Re \sqrt{\frac{d}{2 R_c}} \quad (1.17)$$

Where  $Re$  is the Reynolds number,  $d$  is the diameter and  $R_c$  is the radius of curvature.

A valid assumption for the haemodynamic simulations is ignoring the effects of curvatures on the channel damage because they are limited [19].

The wall shear stress ( $\tau$ ) is the mechanical stress in the vessel wall exerted by the flowing blood

$$\tau_{wall} = \mu \frac{du}{dr} \quad (1.18)$$

The ratio  $du/dr$  is the shear rate (measured in  $s^{-1}$ ) and  $\mu$  is the dynamic viscosity that expresses its resistance to flow. If the viscosity depends on the shear rate, the fluid is non-Newtonian, if it doesn't depend on shear rate it is a Newtonian fluid [20] [21].

The relation between WSS and shear rate is linear if the fluid is Newtonian and non-linear if the fluid is non-Newtonian.

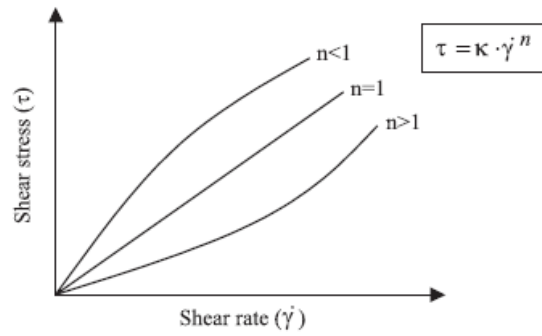


Figure 1.8 Relation between shear rate and WSS in Newtonian fluid ( $n=1$ )  
And non-Newtonian fluid ( $n < 1$  or  $n > 1$ ) [22]

The mean wall shear rate value in cardiac cycle is about  $40\text{-}70\text{ s}^{-1}$  in the ascending aorta and, in smaller arteries, around  $300\text{-}500\text{ s}^{-1}$ . The instantaneous shear rate in the aorta during systolic peak is five times the mean value, in smaller arteries there is a small pulsatile motion, so the instantaneous value is only twice the mean value [4].

#### 1.4 CARDIOVASCULAR PATHOLOGIES

Cardiovascular diseases are a group of heart or blood vessels disorders and are the main cause of death in the world [23]. Main pathologies of blood vessel are thrombosis and atherosclerosis; these pathologies can affect different areas of cardiovascular system, for example peripheral arteries, cerebral arteries and coronary arteries.

In this work, we focused on the coronary arteries that are the vessels responsible of carrying nutrients and oxygen to the heart muscle. They generate from ascending aorta and consist of two main branches: the left coronary artery (LCA) and the right coronary artery (RCA). The first one is subdivided into another two branches, the left anterior descending (LAD) and the left circumflex (LCX); a schematic subdivision of coronary arteries is reported in Figure 1.9.

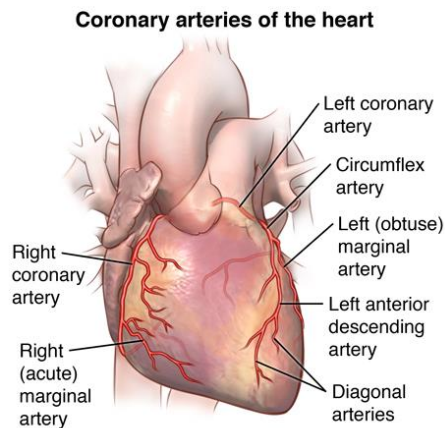


Figure 1.9 coronary arteries [24]

Each branch of the coronary tree supplies blood to a specific region of the myocardium. The American Heart Association subdivides the coronary tree into sixteen segments, it is a good method used by cardiologists to collocate atherosclerotic plaques in coronaries [25].

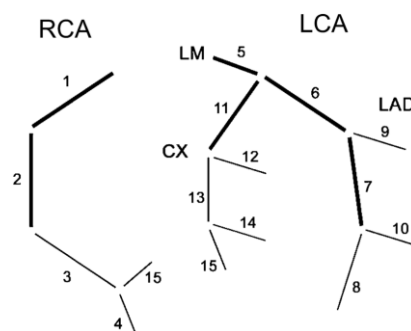


Figure 1.10 16 segments of coronary tree [26]

#### 1.4.1 THROMBOSIS

Thrombosis is a pathological process that gives rise to the thickening of a mass of blood tissue, called thrombus, that adheres to the vessel wall. The presence of a thrombus is dangerous because it can occupy part or the entire vessel lumen, obstructing the blood flow. It causes the lack of oxygen and nutrients to vital organs and tissues, causing necrosis.

Thrombi can be divided into two categories: venous thrombi and arterial thrombi.

Venous thrombi, the so-called red thrombi, are a consequence of blood stasis, for this reason they are rich in erythrocytes.

Arterial thrombi origin especially in a damaged endothelial area; they are white because they are formed by many platelets and fibrin, while there are few RBCs because of the

rapid flow. Thrombi in coronary circulation tend to have a layered structure, each layer has blood material of different age [27].

It has been noted that high values of wall mechanical stress cause the activation of platelets, that tend to aggregate (coagulation), and the probability of thrombi formation increases [28] [29].

In coronary arteries, the formation of platelet-rich thrombi can be the consequence of rupture of atherosclerotic plaques; when it occurs the heart blood circulation is compromised. Thrombosis in coronary arteries is called acute coronary syndrome, that is a coronary artery disease (CAD). It can have fatal consequences, such as myocardial infarction, an ischemic necrosis of cardiomyocytes.

#### 1.4.2 ATHEROSCLEROSIS

Atherosclerosis is a pathology characterized by the alteration of the vessel wall, in particular of the tunica intima. The alteration is caused by the formation of plaques (atheroma) made up of lipids, connective tissue and other substances that can be found in blood. These plaques can harden the artery wall and close the vessel lumen causing stenosis. The core of plaques is composed of thrombotic material, for this reason the rupture of atheroma leads to thrombosis [30]. This phenomenon occurs especially in large arteries (aorta, coronaries, cerebral arteries etc.), where there are bifurcations or compression and flexion areas.

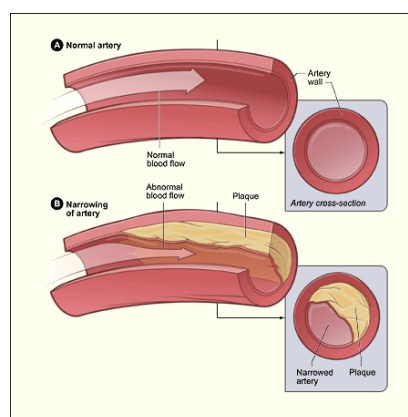


Figure 1.11 Differences between a normal artery and an artery with atherosclerotic plaque [31]

Atheromatic formation begins from the infiltration of LDL (low density lipoprotein) in the endothelium. This phenomenon is regulated by LDL receptors whose synthesis is led by the quantity of cholesterol; for this reason, one of the main systemic causes

of atherosclerosis is hypercholesterolemia. In the endothelium, LDL is oxidised and modified by enzymatic attacks, causing the enrolment of macrophages.

Macrophages act phagocytosis and they evolve into foam cells causing inflammatory processes. These processes are recognised as endothelium damage, so the endothelial activation leads to the production of cytokines which, through molecule-1 (VCAM-1) vascular cell adhesion, recall monocytes and leukocytes. The accumulation of lipids (fatty streaks) becomes a fibrotic plaque because of the migration and proliferation of smooth muscle cells. Lipids in the plaques stimulate the production of growth factors, that normally are not present in vessel wall. Therefore, smooth muscle cells secrete extracellular matrix forming a fibrotic capsule. In this capsule some macrophages die, releasing extracellular lipids and contributing to the formation of lipid core, that is highly thrombogenic. In some atherosclerotic lesions it is likely to find calcium nodules. Because of the thrombogenic nature of lipid core, the plaque rupture can lead to aggregation, adhesion and platelets activation [32]. Coronary artery disease (CAD) is the main cause of cardiovascular mortality (>4.5 deaths in developing word) and he number of deaths for cardiovascular pathologies is increasing [33].

The exact causes of CAD are still not clear, but it is possible to identify many risk factors involved in the CAD development; some risk factors are controllable and the controlling is a good prevention method, while other risk factors cannot be controlled [34].

Uncontrollable risk factors are:

- Aging;
- Gender (the risk of developing CAD is higher for male);
- Genetic factors;
- Ethnic group.

Controllable factors are [31] [33]:

- Hypercholesterolemia (a condition of high LDL cholesterol and low HDL cholesterol);
- Hypertension;



- Smoking;
- Diabetes;
- Obesity;
- Lack of physical activity.

Symptoms of atherosclerosis are not evident during the early state of the pathology, but, in an advanced state, atherosclerosis can cause unexpected heart attacks or strokes. In general, the onset of symptoms depends on the affected arteries.

For coronary arteries the main symptom is angina: it is essentially a chest pain caused by the deficit of oxygen in the heart muscle (ischemia). Other symptoms can be arrhythmias, shortness of breath and lack of energy [31]. Ischemia is caused by the narrowing of vessel lumen and consequent reduction of oxygenated blood flow; this pathology presents three levels of seriousness: angina pectoris that is intermittent, chronic and acute, that is myocardial infarction.

Another risk factor can be the artery geometry: each patient has a different geometric shape of vessels and this factor influences the blood flow. Plaque formation is improved in areas with inner curvature or bifurcation because these kinds of geometries create separation and turbulent flow and areas with low wall shear stress [35] [36].

WSS distribution in arterial flow is particularly relevant in vascular diseases, specifically in atherosclerosis; there is a statistical correlation between atherosclerosis development and specific WSS conditions. Studies show that regions with low or oscillating WSS cause the development of atherosclerotic plaques [37] [38]. Another model study demonstrated the correlation between wall shear stress and the intimal wall thickening [39]: the intima thickness increases significantly in the low-shear sites. WSS values can also determinate a change in the morphology and orientation of endothelial cells of cytoskeleton creating adhesion plaques [40].

The coronaries system presents significant curvatures which cause the velocity shift from axial position to the external wall and the consequent generation of Dean's flow with low value of wall shear stress.

Additionally, the vessel wall thickness increases in the external side of curvature and it promotes the formation of atheroma in these regions.

## CLASSIFICATION

The American Heart Association (AHA) developed a strategy to classify atherosclerotic lesions based on the structure and the composition of plaques. The accumulation of lipids in the tunica intima is the starting point of lesions, the gradual increment of lipids caused the increase of dimension and complexity of lesions.

The lesion classification can be stable, or it can advance in presence of stimulus over time. Each step has different histological characteristics.

- TYPE I: lesions characterized by lipid deposit detectable only by microscope or with chemical agents. This kind of lesions is typical of new-borns; adults have these lesions in areas less subject to atherogenesis.
- TYPE II: lesions are visible and composed principally by macrophage foam cells stratified in adjacent layers, for this reason lesions appear as yellow-coloured streaks. This kind of lesions manifests itself during the years of puberty.

There is an additional subdivision of type II lesions. Type II-a (progression-prone) includes lesions located where the intima is thicker and represents the step before the transition to type III.

Type II-b (progression-resistant) lesions are located in areas where the intima is thin, with less smooth muscle cells. This type doesn't tend to progress, or the transition is very slow [41].

- TYPE III: lesions are characterized by pooling of macroscopic extracellular lipids. They are typical of young adults.
- TYPE IV: it is the first step of advanced lesions, characterized by deposits of extracellular lipids that influence the intima structure. Deposits occupy well-defined areas of intima forming the so-called lipid core of atheroma and narrowing the vessel lumen.
- TYPE V: the main characteristic of this type of lesions is the high deposit of fibrous connective tissue. It is a replacement of damaged vessel tissues and it is the external layer of atheroma. This type of lesions can have calcifications in the lipid core in some cases.

- **TYPE VI:** it is the category of the most complicated lesions that present endothelial surface flaws, haematoma-haemorrhage and thrombosis. These lesions appear after the fourth decade in life.

The lesions formation in coronary arteries speeds up from 25-30 years old for male and from 40-45 years old for female and the composition of lesions becomes unpredictable starting with the third decade [4].

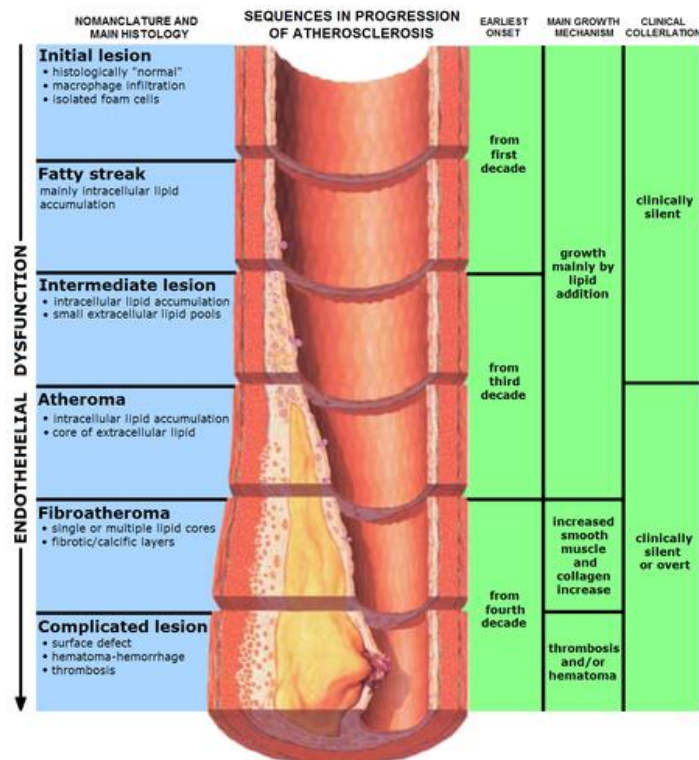


Figure 1.12 The progression of atherosclerosis [42].

### 1.4.3 SECONDARY PATHOLOGIES

Secondary pathologies are vascular diseases that originate from atherosclerosis. One of the most serious pathologies is the acute coronary syndrome, caused by the formation of a large thrombus that obstructs the vessel lumen.

Another pathology is the acute thrombosis caused by the plaque breakage: the contact between lipid core and blood induces platelets activation. Other pathologies derived by atherosclerosis can be heart infraction, ischemia and heart attack.

In conclusion, atherosclerosis is a pathology that can trigger a lot of fatal diseases, therefore it is important to have accurate diagnosis methodologies for a good prevention.

## 2 ANALYSIS OF ATHEROSCLEROSIS

The diagnosis of atherosclerosis is based on the evaluation and analysis of risk factors, but this is not enough; it is necessary to use appropriate medical examinations to have an accurate diagnosis of the pathology.

### *2.1 IMAGING TECHNIQUES*

Indirect diagnostic methods, such as electrocardiogram (ECG) and echocardiography, only tell if the disease is present or not. Direct tests are based on imaging techniques and they give indications about the presence of atherosclerosis and its state of progress.

#### *2.1.1 CORONARY ANGIOGRAPHY*

Coronary angiography (CA) is an exam that is used to control the morphology of blood vessels, to see if there are any lumen narrowing and to study the blood flow. It is a diagnostic method based on the use of X-rays: through a peripheral artery, a catheter is inserted, it reaches the coronary arteries and there a substance called contrast agent is introduced. Contrast agent contains iodine, it modifies the mean atomic number or the density of the blood and consequently its capacity to absorb photons X. By doing so it is possible to distinguish blood vessels from muscle tissues [43]. CA is an imaging minimal invasive procedure that gives a temporal sequence of 2D images (dynamic images) and it doesn't allow to evaluate the condition of vessel walls and potential plaques. Being invasive, this technique introduces risks during the procedure.



*Figure 2.1 Instant image of coronaries during a coronary angiography [44]*

### *2.1.2 INTRAVASCULAR ULTRASOUND*

Intravascular ultrasound (IVUS) is an invasive method similar to the angiography. An ultrasound probe is attached to the end of the catheter and the latter is introduced and it arrives to the coronary arteries through a peripheral artery. The probe extraction occurs with a constant velocity and it rotates capturing images and measuring the sound waves reflection on blood vessels. The advantage over the angiography is that the IVUS doesn't give only a 2D visualization of blood vessels, it allows the visualization of the entire vessel wall, the plaque size and its composition. Other advantage is the very good spatial and temporal resolution [45]. The main disadvantage is that validated methods for an objective and automatic classification of atheroma do not exist; the interpretation has to be based on a visual inspection of acoustic reflection [45]. Furthermore, the analysis of a significant stenosis is not possible because of the diameter of the ultrasound probe [46].

### *2.1.3 COMPUTED TOMOGRAPHY*

Computed tomography was introduced in 1970s and it was a revolution for medical imaging. It is a non-invasive method and, differently from angiography, it includes information about vessel walls and it has high 3-dimensional spatial and temporal resolution [47].

Essentially, a TC system is composed by a scanner that plays a fundamental role in reconstructive imaging, a computerized calculation system and a system of display for image manipulation. Output images of TC are multiple slices of cross area of the involved part of the body, it is very useful for the 3D images elaboration. Each slice represents a section with a specific thickness, the number of slices depends on the distance between sections.

The TC scanner has an X-ray tube: X-rays are characterized by wavelength ( $\lambda$ ) and energy (E): when rays interact with tissues, they lose energy. The aptitude of tissue to absorb X-rays depends on the attenuation coefficient  $\mu$ , that is different in each tissue. CT images are a representation of the attenuation coefficient distribution: each pixel of the image represents absorption characteristics of a small volume.

X-rays used in medical diagnostics have a frequency about  $3 \cdot 10^{18}$ -  $3 \cdot 10^{19}$  Hz and a wavelength about 0.01-0.1 nm [43].

There is no absolute unit of measure for the measuring of the value of the attenuation coefficient; instead it is employed a scale based on the water attenuation, called Hounsfield Units (HU). By doing so, the attenuation of soft tissues is near 0 HU, while for example, bone tissue has an attenuation of around 1000 HU.

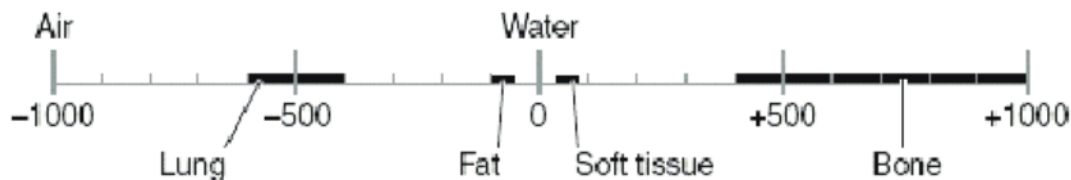


Figure 2.2 The Hounsfield scale of TC numbers [48]

#### 2.1.4 OPTICAL COHERENCE TOMOGRAPHY

Optical coherence tomography (OCT) is a non-invasive diagnostic technique that uses low-coherence interferometry to obtain cross-sectional images. The images are obtained from the internal tissue optical scattering: in other words, it is a measure of biological tissues optical reflections. This technique has a longitudinal and lateral resolution of few micrometer [49]. It is usually used in ophthalmology, but some studies show the application of this method in cardiovascular medicine [50] [51] [52]. The result of the Brezinski's study shows that OCT allows a precious differentiation of vascular tissue. In general, the three studies mentioned show the good results about the application of OCT in cardiovascular system, especially in coronary arteries.

## 2.2 FUNCTIONAL CLINICAL ANALYSIS

#### 2.2.1 FRACTIONAL FLOW RESERVE

Fractional Flow Reserve (FFR) is the gold standard to evaluate the functional assessment of coronary stenosis, especially in stable coronary artery diseases. The most important study about FFR is the FAME [53] and the FAME 2 [54] demonstrated the advantages of using this indicator in the evaluation of stenosis severity.

Using diagnostic techniques such as coronary angiography, the evaluation is completely subjective and this limits the accuracy of the exam.

FFR is the ratio between the mean pressure downstream of a stenosis and its mean upstream pressure during hyperaemia. In other terms, it is the portion of the flow that is preserved despite stenosis. There are two formulations of the FFR formula: the first is the complete one (2.1), while the second one (2.2) has the same significance but some terms have been neglected.

$$FFR = \frac{(P_d - P_v)/R_{myo}}{(P_a - P_v)/R_{myo}} \quad (2.1)$$

$$FFR = \frac{P_d}{P_a} \quad (2.2)$$

$P_d$  is the pressure downstream of the stenosis,  $P_v$  is the atrial pressure,  $P_a$  is the aortic pressure that undergoes small variations and  $R_{mio}$  is the resistance of myocardium [55].

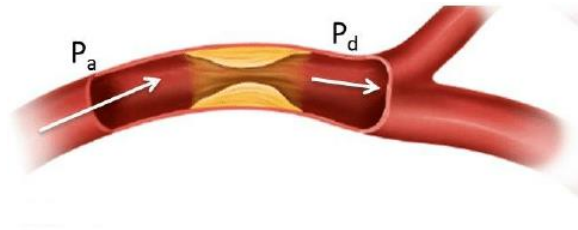


Figure 2.3 Fractional Flow Reserve [56]

The value  $FFR=1$  represents a normal vessel while, if  $FFR<1$ , there is a stenosis in the vessel.

The FFR cut-off value is considered 0.8 [53] [54]:

- $FFR \leq 0.8 \rightarrow$  the lesion has to be treated.
- $FFR > 0.8 \rightarrow$  the lesion is not critical.

Measurements for the evaluation of FFR are essentially invasive but a non-invasive alternative exists: the virtual fractional flow reserve (vFFR). It is based on the construction of a coronary arteries model starting from a set of TC images. Combined with the anatomical model, the CFD analysis is used and vFFR can be determined by solving equations of blood flow for the velocity and pressure. The final result is a spatial distribution of FFR [57] [58], but it is affected by some problems.

First of all, CT images can be noisy, limiting the accuracy of model reconstruction and, as a consequence, the accuracy of the FFR value. A second problem is the used fluid dynamic model: it can be inaccurate in specific subjects. Finally, simulation parameters have a margin of error caused by the variability between patients. In conclusion, fractional flow reserve is a useful method to take the right decision about taking action or not in a vessel lesion.

### 2.2.2 INSTANTANEOUS WAVE-FREE RATIO (iFR)

Instantaneous wave-free ratio is a functional parameter used for the study of coronary stenosis and their severity. iFR is obtained measuring the intracoronary diastolic pressure upstream and downstream the stenosis; during the diastole microvascular resistances are minimal (wave-free period) [59]. The advantage of this method is that is possible to obtain instantaneous stenosis evaluation without inducing hyperaemia. Comparing the diagnostic accuracy of FFR and the one of iFR, both measures have similar accuracy [59].

### 2.2.3 CORONARY FLOW RESERVE (CFR)

Coronary flow reserve is a flow-based indicator and it represents the efficiency of the coronary circulation to increase the blood flow, as a response to an increase of oxygen demand. It is used to evaluate the microcirculation. The so-called absolute CFR is the ratio between the average peak velocity during maximal hyperaemia (APV<sub>h</sub>) and the average peak velocity at baseline condition (APV<sub>b</sub>) [60].

$$CFR = APV_h / APV_b \quad (2.3)$$

Another kind of CFR is the relative coronary flow reserve, which is the ratio between the maximum flow in a diseased artery and the maximum flow in a healthy artery [61].

The difference between CFR and FFR is represented in figure 2.4.



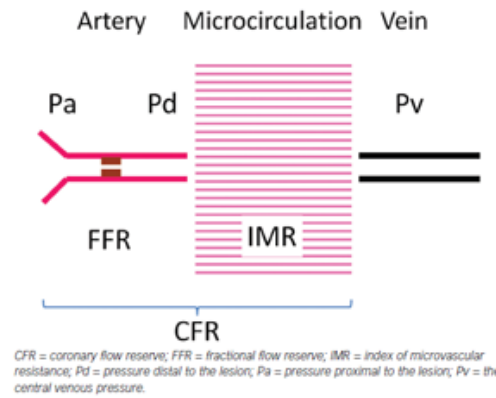


Figure 2.4 FFR and CFR [62]

The average CFR value is about 2.7 in humans and the cut-off value for clinical practice is 2.0 [60].

Combining FFR and CFR it is possible to establish a plan of diagnosis and treatment; the IMR (Index of Microvascular Resistance) is not considered in the following figure, as more information is needed to establish a cut-off value.

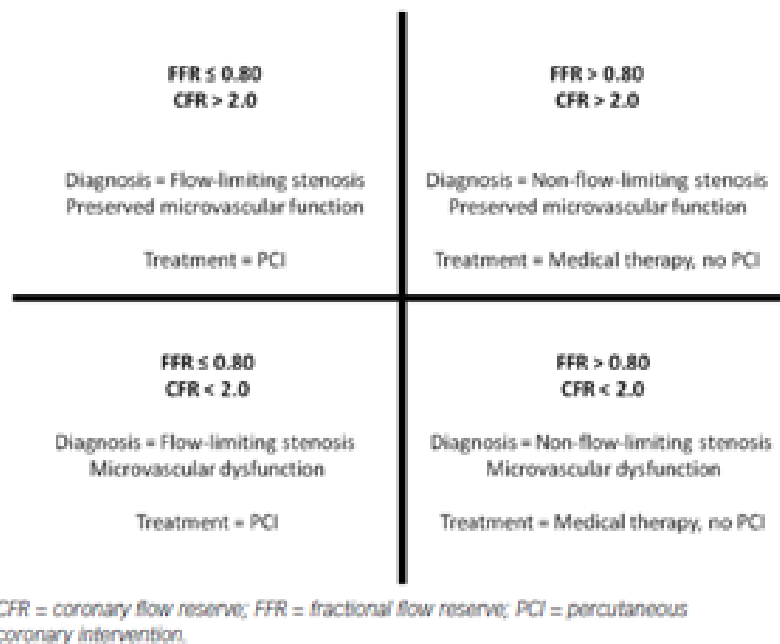


Figure 2.5 Diagnosis and treatments plan based on FFR and CFR [62].

## 2.3 CFD ANALYSIS

Computational fluid dynamics (CFD) is the analysis of system involving fluid flow by means of computer-based simulations [63]. In bioengineering, CFD can be used as a diagnostic tool, as a support tool in patient treatments and as a basic tool to the study of fluid-structure interactions. CFD, combined with cardiovascular imaging, is used for the characterization of complex physiological flow and pressure fields in presence of stenosis; physics and mathematical laws are used to simulate the blood flow through cardiovascular system.

Frequently, cardiovascular images are captured with invasive methods but, using CT images, it is possible to apply a non-invasive approach.

A patient specific CFD simulation could be synthesized in eight steps [64]:

- 1 Images acquisition with CT scan;
- 2 Segmentation and reconstruction of 3D model from images: a smoothing filter has to be applied to the model;
- 3 Spatial discretization: the volume is divided into several tetrahedral cells and the whole of elements is called mesh. The mesh quality is associated to the regularity of elements and it has a fundamental influence on the simulation results, but a too refined mesh has a negative impact on computational resources and time solution;
- 4 Temporal discretization: the number of time steps of the solution has been set;
- 5 Pre-processing: application of boundary conditions. As it is not possible to discretize the whole cardiovascular network, only the region of interest is reconstructed and, at inlet, outlet and on the wall, physiological conditions are imposed. Boundary conditions can be based on patient-specific data, physical models or population data;
- 6 Simulation: during this step the CFD solver, using parameters and information provided by the operator, simultaneously and repeatedly solves Navier-Stokes and continuity equations over all elements;
- 7 Results post-processing: the operator can extract data of interest as general pressure and velocity of fluid. Additional data can be Wall shear stress map that normally is difficult and invasive to measure;

8 The last step is the validation that is the comparison of CFD results with, for example, in vivo measurements.

The application of CFD in the cardiovascular system involves uncertainties because the creation of the three-dimensional models is based on some approximations. There are errors associated with the discretization of the partial differential equation in time and space, others are convergence errors caused by the finiteness of iterations and elements.

Other uncertainties are introduced by assumptions about blood and mechanical properties of the vessel walls: blood is modelled as a Newtonian incompressible fluid and walls are considered rigid.

### 2.3.1 GOVERNING EQUATIONS

CFD is based on the numerical solution of a system of partial differential equations which govern the fluid motion known as Navier-Stokes equations. For an incompressible and Newtonian fluid, the equations for mass and momentum conservation are reported respectively in 2.4 and 2.5:

$$\nabla \cdot \mathbf{u} = 0 \quad (2.4)$$

$$\frac{\partial \mathbf{u}}{\partial t} + (\mathbf{u} \cdot \nabla) \mathbf{u} = -\frac{1}{\rho} \nabla P + \nu \nabla^2 \mathbf{u} \quad (2.5)$$

$\mathbf{u}$  is the velocity,  $t$  is the time,  $P$  is the pressure,  $\rho$  is the density and  $\nu$  is the viscosity.

To numerically solve these equations is necessary to discretize the volume: a volume is divided into  $n$  elements and, for each element, the computer solves the system of equations. This group of methods is called finite element techniques [65] [66].

To define a fluid flow problem, the system of equations has to be combined with appropriate boundary conditions (BCs).

The two main kind of boundary conditions used in computational haemodynamic are:

- Dirichlet BCs impose the value of the solution at the domain boundaries;
- Neumann BCs impose the value of the derivative of the solution at the domain boundaries.

The strong form of N-S equations is

$$\begin{aligned}\rho \vec{v}_t + \rho \vec{v} \cdot \nabla \vec{v} &= -\nabla p + \text{div}(\tau) + \vec{f} \quad \forall x \in \Omega \\ \forall x \in \partial_g \Omega: v_i &= g_i \\ \forall x \in \partial_h \Omega: -pn + \tau_{ji} &= h_i\end{aligned}\tag{2.6}$$

The boundary of the fluid domain is divided into a Dirichlet portion ( $\partial_g \Omega$ ) and a Neumann portion ( $\partial_h \Omega$ ) [67].

There is also a weak form that is

$$\int \rho \vec{w} \cdot (\vec{v}_t + \vec{v} \cdot \nabla \vec{v} - \vec{f}) d\Omega = \int \vec{w} \cdot (-\nabla p + \nabla \cdot \tau) d\Omega \tag{2.7}$$

### 2.3.2 TYPE OF BOUNDARY CONDITIONS

To obtain high quality cardiovascular simulation results, is fundamental to define BCs are defined as accurately as possible. There are a lot of approaches to assign boundary conditions to a 3D model. Essentially, three classes of boundary conditions exist:

- In vivo measured BCs;
- Lumped Parameters Models (LPM)
- Scaling law-based boundary conditions.

#### *IN VIVO MEASURED BCs*

It is possible to extract the BCs from in vivo measurement of blood flow rates; using these measurements, the boundary conditions are patient-specific. Some studies on the human aorta [68] [69] imposed boundary conditions obtained from 4D phase contrast MRI. In other studies, intravascular doppler ultrasound has been used to determine the blood flow velocity, so the flow rate can be calculated if the cross-sectional area is known [70] [71].

#### *LUMPED PARAMETERS MODELS*

Many Lumped Parameters Models exist, but it was decided to treat those most used in literature.

The simplest lumped parameters model is RCR Windkessel model that is a 0D reduced model coupled to the 3D model and described by a set of ordinary differential equations. In this model the vascular behaviour is represented by three parameters: a proximal resistance ( $R_p$ ) that represents the viscous arteries resistance downstream the model,  $C$ , the capacitance that represents the vessel compliance and  $R_d$ , the resistance of the systemic circulation.

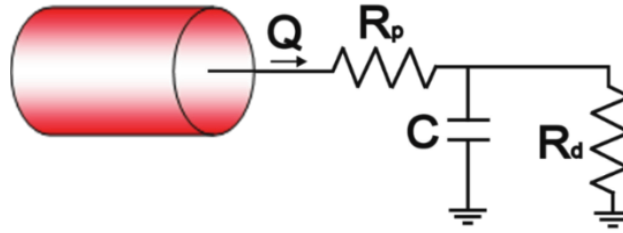


Figure 2.6 RCR Lumped Parameters Model [72].

Generally, this model is applied to aortic outlet or inlet, while another model is employed for coronary arteries outlet. In the study ran by *H.J.Kim et al.* [73] the coronary lumped parameter model has been introduced.

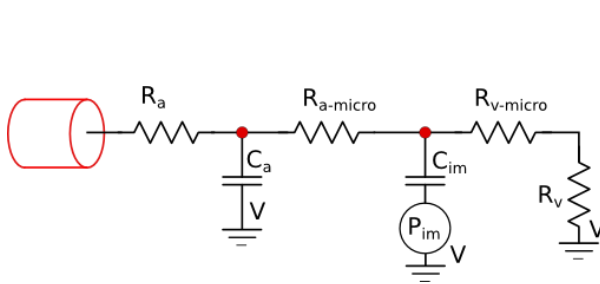


Figure 2.7 Coronary LPM [72]

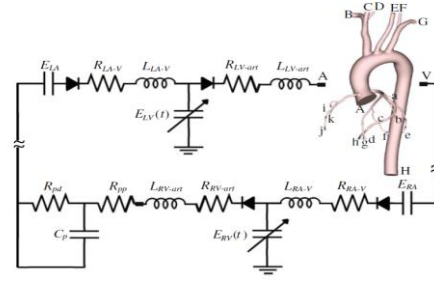


Figure 2.8 Closed loop system for heart model [73]

#### Parameters:

- $R_a$  is the arterial resistance
- $C_a$  is the microcirculation compliance
- $R_{a-micro}$  is the microcirculation resistance
- $R_{v-micro}$  is the venous microcirculation resistance
- $C_{im}$  is the myocardial compliance
- $R_v$  is the venous resistance
- $P_{im}(t)$  is the intra-myocardial pressure.

Pressure parameter is one of the most important features and it can change according to the location of the coronary bed. Its value is obtained from a heart lumped

parameters model; it is a complex closed loop system (Figure 2.8) that allows the switch from left ventricular pressure to the right one.

There are other lumped parameters models that have more parameters; for example, in the study by *Duanmu et al.* [74] all vessel terminals are connected to a structural tree model introduced by *Olufsen et al.*

Therefore, all the terminals of coronary arteries are assigned to a root impedance computed from the structured tree model. Their values are near perfusion resistance measurement results.

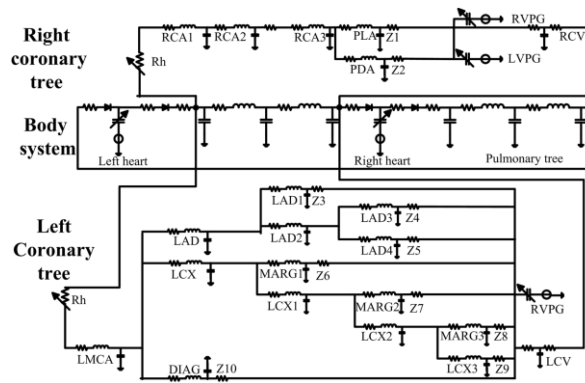


Figure 2.9 Closed loop circulation model [74].

#### SCALING LAW-BASED BOUNDARY CONDITIONS

Other approaches to assign boundary conditions are based on the outflow diameter, volume and myocardial flow measurements. An example is the study by *Van der Giessen et al.*: this work is based on a diameter-based model. It is a comparison between prediction of the flow ratio through the side branches given by Murray's Law (2.8) and the empirical model based on measurements performed by *Doriot et al.* Formula (2.9) is the Doriot's fit [75].

$$\frac{q_{D2}}{q_{D1}} = \left( \frac{d_{D2}}{d_{D1}} \right)^3 \quad (2.8)$$

$$q = k * d^x \quad (2.9)$$

Based on data provided by *Doriot et al. [76]* two relations have been obtained:

$$\frac{q_{D2}}{q_{D1}} = \left( \frac{d_{D2}}{d_{D1}} \right)^{2.27} \quad (2.10)$$

$$q = 1.43 * d^{2.55} \quad (2.11)$$

Differences between two models are evaluated on WSS values. In bifurcation areas the application of Murray's Law underestimates the size of the region with low WSS compared to Doriot's fit. In non-bifurcation areas Murray's Law overestimates average WSS value compared to Doriot's fit [75].

### 2.3.3 HAEMODYNAMIC DESCRIPTORS

The atherosclerotic diseases are influenced by disturbed flow, for this reason CFD results can be translate into information about the flow, calculating specific descriptors based on the velocities and the wall shear stress that have an important role in the endothelial function and phenotype.

#### WSS-BASED DESCRIPTORS

The main WSS-based descriptors are three: TAWSS, OSI and RRT. Other descriptors exist and are based on the gradient of WSS or on the harmonic content of the WSS.

Time-Averaged Wall Shear Stress (TAWSS) is a surface descriptor based on the integration of each nodal WSS over the cardiac cycle.

$$TAWSS = \frac{1}{T} \int_0^T |WSS(s, t)| * dt \quad (2.12)$$

To evaluate TAWSS values and their impact on the arteries, threshold values exist [77].

- TAWSS < 0.4 Pa (4 dyne/cm<sup>2</sup>): values that characterize atherosclerosis-prone areas;
- TAWSS > 1.5 Pa (15 dyne/cm<sup>2</sup>): values considered atheroprotective;
- TAWSS > 10-15 Pa (100-150 dyne/cm<sup>2</sup>): in this case the elevate forces can damage the endothelium.

The Oscillatory Shear Index (OSI) is a parameter that indicates the extent of the WSS oscillation during cardiac cycle [78].

$$OSI = 0.5 \left[ 1 - \left( \frac{|\int_0^T WSS(s,t) * dt|}{\int_0^T |WSS(s,t)| * dt} \right) \right] \quad (2.13)$$

It is between 0 and 0.5 [79]:

- Low OSI values indicate a slightly disturbed flow and a minimal deviation of instantaneous WSS from the main flow direction;
- High OSI values indicate areas where the flow is more perturbed and the instantaneous WSS does not follow the main direction of the flow, it perturbs the endothelial conformation.

The Relative Residence Time (RRT) is expressed as

$$RRT = \frac{1}{(1-2 \cdot OSI) \cdot TAWSS} \quad (2.14)$$

It is related to the permanence time of the fluid particles near the wall [68].

#### *BULK-FLOW DESCRIPTORS*

The intravascular structures are 4D phenomena and the descriptors have to operate a reduction of complexity of the flow fields. The role of the bulk flow in the arterial diseases, specifically in the coronary arteries, has been studied by *De Nisco et al. [80]*.

One of the principal bulk flow descriptors is the helicity: it is a scalar value that describes the connection between the complexity and the energy. It is useful to study the development of structures that rotate while being transported. Helicity measures the alignment of velocity and vorticity ( $\vec{w} = (\nabla \times \vec{v})$ ), where vorticity is the rotation axis of a fluid element.



The descriptor for helicity is the Density of Kinetic Helicity and it is expressed by the formula 2.15 [79].

$$h(s, t) = \vec{v}(s, t) * \vec{w}(s, t) = \vec{v} * (\nabla \times \vec{v}) = |v| * |w| * \cos\varphi \quad (2.15)$$

$\varphi$  is the angle between the velocity vector and vorticity vector.

The Local Normalized Helicity (LNH) is defined by formula 2.16 and it is calculated in each point of element trajectory [79].

$$LNH(s, t) = \frac{\vec{v}(s, t) * \vec{w}(s, t)}{|v(s, t)| * |w(s, t)|} = \cos\varphi(s, t) \quad -1 < LNH < 1 \quad (2.16)$$

Starting from the LNH it is possible to obtain other indicators:

- $Hfi_k$  is the helicity index for the k-th trajectory and depend on the LNH;
- HFI is the Helical Flow Index that is the helicity index that considers all particles, it is between 0 and 1.

$$HFI = \frac{1}{N_p} \sum_{k=1}^{N_p} hfi_k \quad (2.17)$$

Based on vorticity, it is possible to calculate other bulk flow descriptors. The Vorticity component Ratio Index (VRI) that is the ratio between the vorticity component parallel to the velocity and the component orthogonal to the velocity.

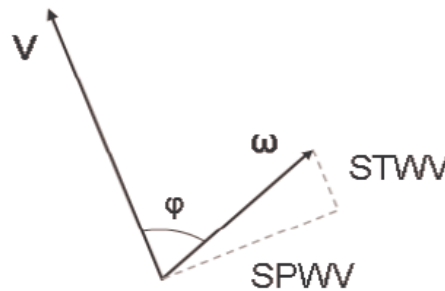


Figure 2.10 – Vorticity components [79].

STWV is the streamwise vorticity while SPWV is the spanwise vorticity; they are calculable for each point of a trajectory.

$$vri_k = \left( \frac{stwvi_k}{spwvi_k} \right) \quad (2.18)$$

$$VRI = \frac{1}{N_p} \sum_{k=1}^{N_p} vri_k \quad (2.19)$$

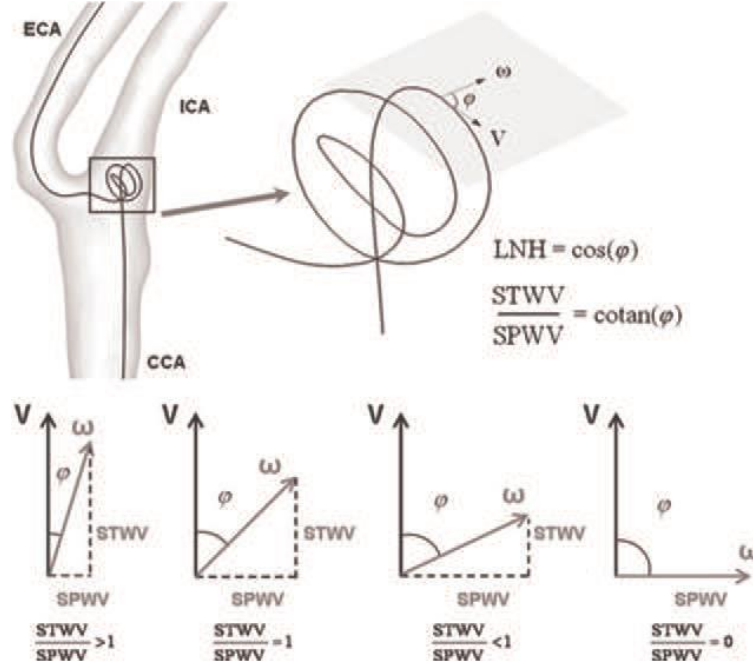


Figure 2.11 – A graphic representation of bulk-flow based descriptors [79].

To evaluate the bulk flow in terms of helical content and flow topology, a group of Eulerian descriptors exist: they give an analysis of the size and the rotational direction of helical flow structures.

The first four of these descriptors are the following [81]:

$$\begin{aligned} h_1 &= \frac{1}{TW_i V_i} \int_{TW_i} \int_{V_i} H_k dV dt \\ h_2 &= \frac{1}{TW_i V_i} \int_{TW_i} \int_{V_i} |H_k| dV dt \\ h_3 &= \frac{h_1}{h_2} \\ h_4 &= \frac{|h_1|}{h_2} \end{aligned} \quad (2.20)$$

$H_k$  is the helicity density, it is integrated over defined time intervals  $TW_i$  of the cardiac cycle and the volumetric fluid domains  $V_i$ .

- $h_1$  is the time-averaged helicity normalized with the volume; a  $h_1$  value near zero indicates the presence of symmetry in the fluid domain.
- $h_2$  is the helicity intensity, it does not depend on the direction and describes the total quantity of helical flow in the fluid domain.
- $h_3$  is a non-dimensional quantity being the ratio between  $h_1$  and  $h_2$ ; its value is between -1 and 1: when  $h_3 = 0$  it is a case of symmetry, if it equals 1 or -1, in the domain, only right-handed or left-handed helical structures are present.
- $h_4$  is the absolute value of  $h_3$ ; it is between 0 and 1 and it is only a balance between counter-rotating structures, the direction is not considered.

The study about the helical flow in coronary arteries [80] highlights the presence of counter-rotating bi-helical structures in the blood flow and their atheroprotective role in the coronary tree.

# 3 MODELS CONSTRUCTION

Since the aim of this project was to evaluate the impact of the assumption of circular section on coronary arteries haemodynamic, four three-dimensional models were reconstructed. In particular, starting from CT images the realistic vessel geometries were obtained for a left and a right coronary artery. Starting from these models other two models were obtained, based on physiological vessels centerlines with the assumption of circular cross-sections. This chapter presents reconstruction methods and the setting of parameters for simulations.

## 3.1 IMAGES ACQUISITION

The set of images is composed by 256 CT images in DICOM format, acquired with a TC scan with the following parameters set:

- Voltage output of X-ray tube KVP: 120;
- Space between slices: -0.625 mm;
- Slice thickness: 0.625 mm;
- Distance between the centre of each pixel: 0.488281/0.488281 mm;
- Number of bits stored for each pixel sample: 16;
- Number of rows and columns in the images: 512x512 pixels.

Images acquired are the starting point for the modelling, but it is important to establish what software gives the best reconstruction.

## 3.2 SEGMENTATION

Three different software was tested for segmentation and three-dimensional reconstruction: VMTK (Open Source), ITK-SNAP (Open Source) and Mimics (Mimics, Materialise). Segmentation has been attempted with each program; the goal was to obtain a smooth surface for each coronary model, without corners, that can alter the results of simulations.

### 3.2.1 VMTK SEGMENTATION

First of all, to work on VMTK it is necessary to convert DICOM images in an image volume (.vti), then the VOI (Volume of interest) was extracted. There are many strategies for the segmentation:

- *Vmtkmarchingcubes* generates an isosurface for a given gray level. It is not a good method for the construction of a vascular model, because a single level generally is not enough to represent the interface between vessel and blood. Also, with this method, building only the vessels of interest is not possible, as all vessels in the VOI are considered.
- *Vmtklevelsetsegmentation* presents an interactive initialization. By choosing *Colliding Front* as initialization method, it is necessary to set a lower and a higher threshold values and then two seeds have to be placed: one at the beginning and one at the end of the branch of interest. A front starts from each seed until the two fronts collide; when it occurs, the initial deformable model is obtained. Parameters to control the deformation of level set are later requested and, after imposing iterations it is possible to proceed with the segmentation of another branch. The result of this segmentation is an image at zero-level and *vmtkmarchingcubes* has to be applied to obtain the surface.

More attempts of segmentations with this latter method have been done but the accuracy and the precision of models obtained was not considered satisfactory.

### 3.2.2 ITK-SNAP SEGMENTATION

ITK-SNAP is a software which allows the direct importation of DICOM images. The set of images is displayed in three plans: orthogonal, coronal and sagittal and it is possible to regulate the contrast to have the best view possible.

Before the segmentation, a region of interest was chosen and resampled by a factor of two with linear interpolation to improve images quality.

Two different pre-segmentation methods were tested:

- *Threshold-based method;*
- *Classification method;*

The first one is based on the choice of two threshold values and a smoothness value, it is a subjective method.

Many attempts have been made using different values of threshold: the lower starting value is 115.0 and the upper value is 550.0 with a smoothness equal to 3.00.

The second method is based on the identification of different tissues to train the classifier; the latter identifies the regions with the same intensity value based on the first manual identification. Once the classifier is trained, it is possible to choose the tissue that is to be segmented.

After the pre-segmentation step, the following step is to place 3D *bubbles* with a variable diameter in the regions of interest to mark the starting values of the algorithm. When the algorithm starts, seeds expand to the neighbouring pixels which satisfy imposed criteria. Before running the segmentation, the configuration of the parameters of the contour evolution differential equation is necessary. The default method weights the parameters regarding their impact on the evolving contour behaviour; the expert one permits to specify the weights in a generic evolution formulation.

An attempt of model reconstruction has been done with this software, but the results were not satisfying.

### 3.2.3 MIMICS SEGMENTATION

The best results were obtained with the coronary segmentation tool of Mimics; it is a semi-automatic method based on start and end points provided by the operator.

First, the algorithm extracts coronary paths and then it segments coronary arteries creating coronary masks. The default output masks include vessel lumen and calcification together, but it is possible to separate the calcifications adjusting the threshold value.

For our models, calcifications have been separated, so we obtain two coronary masks and a mask for each calcification.

Mimics allows to edit masks with three manual methods:

- *Draw*: it is possible to add pixels to the active mask;
- *Erase*: it permits to remove pixels to the mask;
- *Threshold*: it is used to set a local threshold.

There are also automatic operations on the mask morphology:

- *Erode*: delete automatically pixels from the edges;
- *Dilate*: add automatically pixels from the edges;
- *Open*: an erosion immediately followed by a dilatation;
- *Close*: a dilatation immediately followed by an erosion.

With these operations is possible to set some parameters, such as the number of pixels involved in the process, the name of the new mask and the connectivity. The latter parameter can be set on 8-connectivity that looks at the neighbouring pixels in the plane and on 26-connectivity that looks at the neighbouring pixels in 3D.

For our model, first we applied the *Dilate* operation to the coronary masks setting the 8-connectivity, then we use the mask smoothing tool filters to remove eventual artefacts in the active masks.

The following step was to calculate the 3D objects using *Custom Quality*: it allows the setting of some parameters showed in figure 3.1.

Calculate 3D Parameters

Quality  
☐ Low ☐ Medium ☐ High ☐ Optimal ☒ Custom

Interpolation method:  
☐ Gray value ☒ Contour

Prefer:  
☒ Continuity ☐ Accuracy

Shell Reduction  
☐ Largest shells: 1

Slices  
Position of first slice: -255,0170 mm  
Position of last slice: -95,6420 mm  
Reset

Matrix reduction  
XY resolution: 2 x 0,4883 mm  
Z resolution: 1 x 0,6250 mm

Smoothing  
☒ Iterations: 2  
Smooth factor: 0,7000  
☐ Compensate shrinkage

Triangle reduction  
☒ Reducing mode: Advanced edge  
Tolerance: 0,0500 mm  
Edge angle: 15,0000 °  
Iterations: 10

Figure 3.1 – Parameters used to calculate 3D coronaries.

The 3D right and left coronary arteries obtained are showed in figure 3.2.

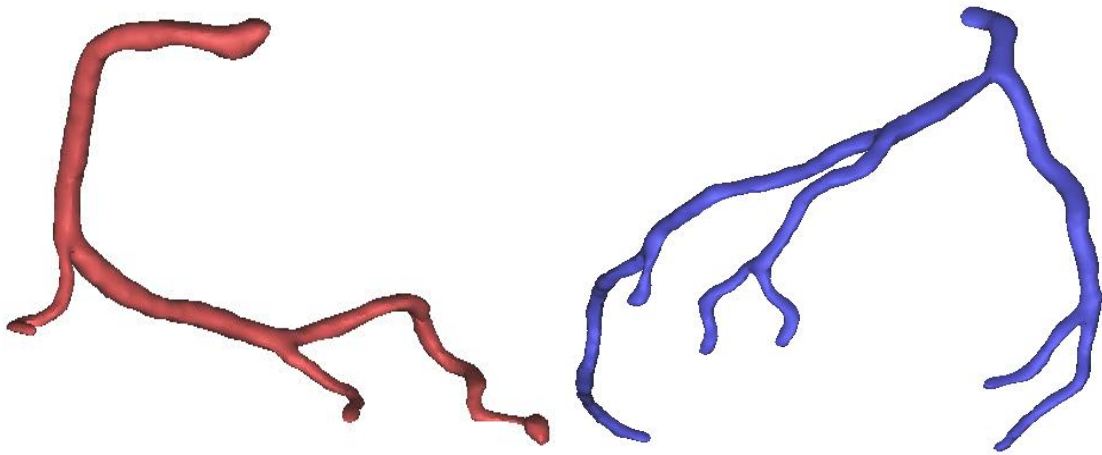


Figure 3.2 – The right and the left coronary arteries after the calculation of the 3D object.

Surfaces are not still smooth: they present corners and imperfections that can alter the simulations, for this reason a second smoothing is necessary. To apply the smoothing filter at the 3D objects it is necessary to set the number of iterations, the smoothing factor and it is possible to choose the option *compensate shrinkage* which prevent the reduction of vessel diameter.

We do not select this option because before, an operation of dilatation has been applied to the masks; without the *compensate shrinkage* the surface is smoother and more regular. To obtain good surfaces but without an excessive diameter reduction, the set of parameters used is:

- Number of iterations: 7;
- Smoothing factor: 0.7.



The results are showed in the following figure.

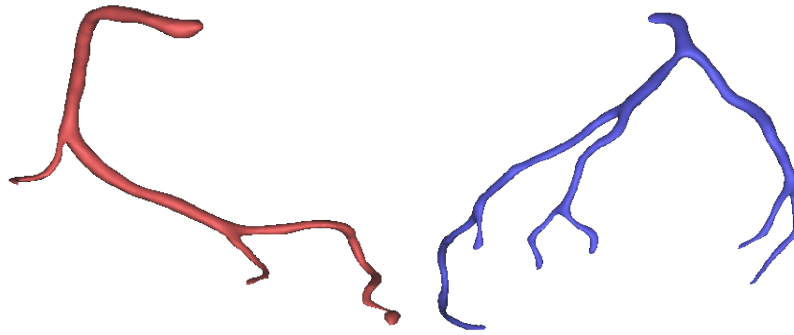


Figure 3.3 – The right and left coronary arteries after the smoothing.

The last step on Mimics was the exportation of the models: the 3D objects were converted in .stl files and saved out of Mimics project.

### 3.3 FINAL MODELS CREATION

A further step was a surface remeshing, to improve the surface mesh quality, with the VMTK script *vmtksurfaceceremeshing*. The parameters imposed were:

- Elements area: 0.01;
- Iterations: 20

Because of the presence of some irregularity on the surfaces, a further smoothing was necessary, so the VMTK script *vmtksurfacesmoothing* was used to refine the models.

The parameters imposed were:

- Number of iterations:100
- Passband: 0.01.

The following step is the *Clipping* of the inlets and the outlets. A first step consists on a manually clipping, with the function *vmtksurfaceclipper*. Starting from the clipped surfaces it is possible to extract the centrelines of each branch.

For our work we need to consider the vessels with diameter greater than 1 mm, for this purpose a Matlab script was implemented.

The script takes in input the centreline of a branch, obtains the curvilinear coordinates and the relation with the radius variation for each point a showed in figure 3.4.

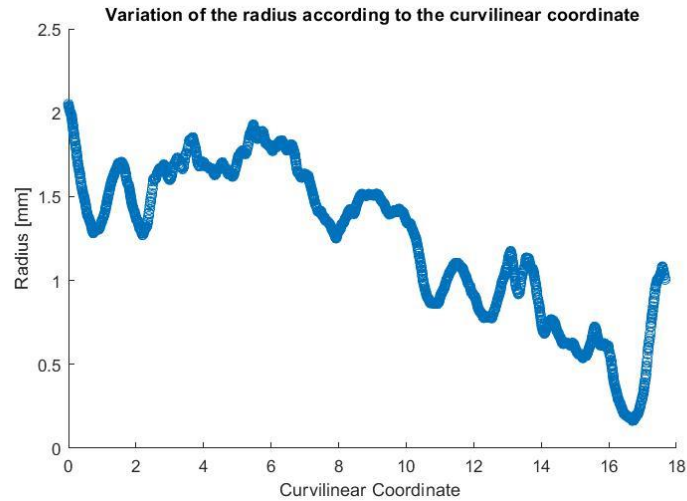


Figure 3.4 – Radius variation in function of curvilinear coordinate for a right coronary branch.

For each branch the script extracts the coordinates of the first point with  $r \leq 0.5$  mm; each point has been used to clip branches in VMTK with the function *vmtpointsplitextractor*. Using this method, it is possible to clip the branches in a specific point of interest and perpendicularly to the centreline.

The final models are displayed in the following figure.

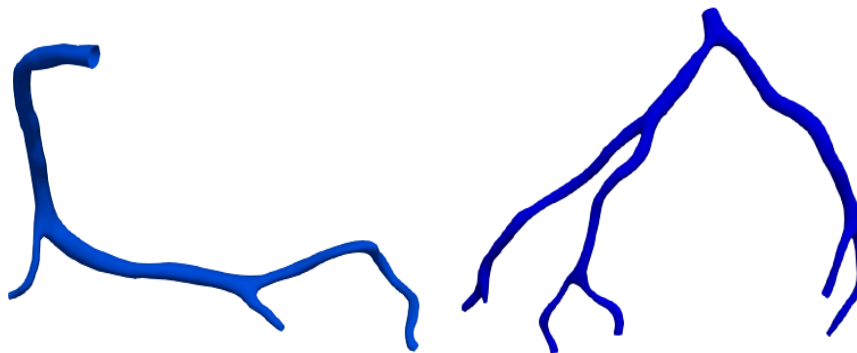


Figure 3.5 – Final physiological reconstruction of right and left coronary artery.

### 3.3.1 CIRCULAR SECTION AREA MODELS

Starting from the centrelines extracted from CT segmented models, the circular section area were reconstructed.

The resampling of centrelines was necessary: different attempts were done to find a length that gives a number of points as close as possible to the number of points of original centrelines.

For the right coronary the best length was 0.052 while for the left one was 0.053. The resampled centrelines are used as input of the function *vmtkcenterlinemodeller*. This function needs other parameters:

- *Radiusarray*: MaximumInscribedSphereRadius;
- *Dimensions*: it represents the resolution of the reconstruction.

For the latter parameter, different attempts were necessary. The starting value was the default value [64;64;64], this value was not enough, so the resolution was increased until a resolution value of [512;512;512]. These models were clipped at the same points of the previous ones. The final results are showed in figure 3.6.

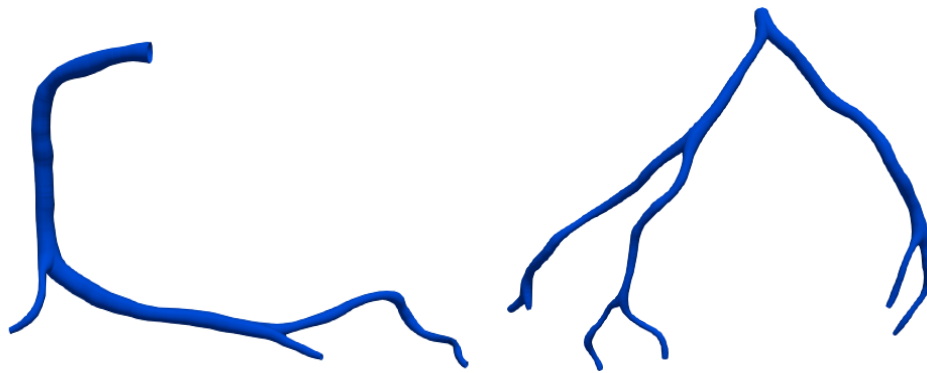


Figure 3.6 – Models with circular section area.

### 3.3.2 MESH GENERATION

Once the models are ready, the volumetric discretization of the models is a fundamental step to proceed with the CFD simulations. This process consists in the subdivision of domain into smaller sub-domains called elements. This step was performed using *SimVascular*, an automatic mesh generator that supports two meshing kernels: TetGen and MeshSim. The latter is a commercial mesher while the first one is an open source program to generate tetrahedral meshes. In this work we used the first one that combines libraries from TetGen and VMTK to provide boundary layers, mesh refinement and radius-based meshing. The mesh generation technique used is the finite-octree method followed by the Delaunay triangulation. The finite-octree method is a decomposition of a complex geometry into more simple elements; after that, elements are meshed using the Delaunay triangulation. The latter defines that no other point in

the triangulation can fall in the circumscribing sphere (circle in 2D) of the points defining a simplex in triangulation. This criterion is showed in figure 3.9.

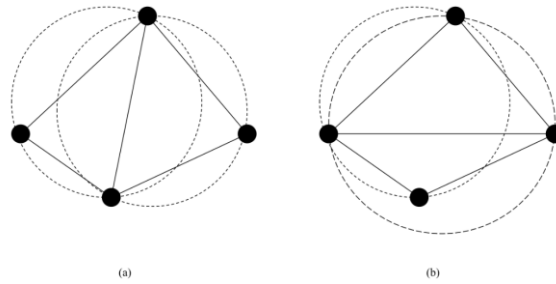


Figure 3.7 – a) Valid Delaunay triangulation; b) non-valid Delaunay triangulation [82].

After the geometry decomposition, the surface meshing is performed applying projected 2D Delaunay surface triangulation. To create the final mesh, templates are used to obtain the volume mesh and 3D Delaunay triangulation is used in the boundary octants. A good quality mesh is important for the simulations: in addition to a visual analysis, there are parameters used by the program to optimize the mesh and improve the mesh quality [82].

The quality indicators are radius ratio, aspect ratio and minimum solid angle and they are showed in figure 3.9.

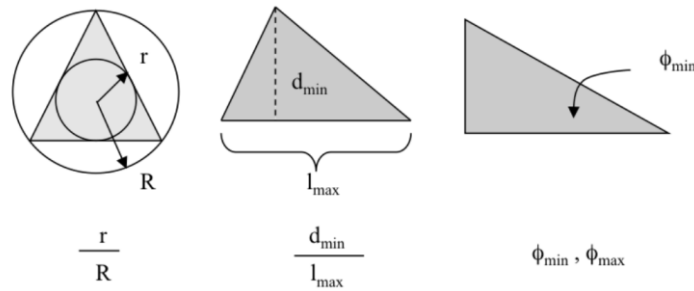
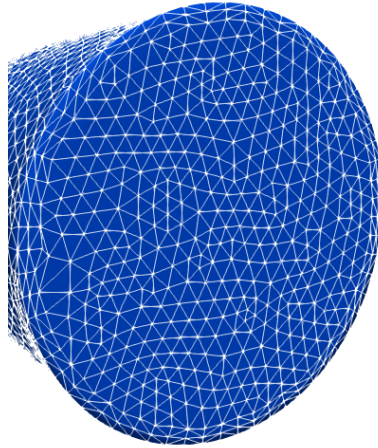


Figure 3.8 – Mesh quality parameters [82].

The tetrahedral mesh size and the boundary layers parameters are user dependent. To achieve the grid independency, a study of mesh sensitivity was performed to find the optimal global edge size.

Two boundary layers with the portion of edge size and the decreasing ratio equal to 0.8 were introduced because of the presence of interesting near walls phenomenon, such as high gradients of pressure or velocity.

An explanatory mesh with boundary layers is showed in figure 3.10.



*Figure 3.9 – Mesh with two boundary layers.*

# 4 SIMULATIONS SETTING

When models are ready, the following step is the study of final simulations setting. To achieve this objective, it is necessary to proceed by steps:

- Flow extension sizing with steady state simulations;
- Mesh sensitivity analysis with steady state simulations;
- The Study of unsteady state boundary conditions;
- The setting of final unsteady simulations.

## 4.1 THE FLOW EXTENSIONS

When fluid enters in a circular pipe with a specific velocity, the particles in direct contact with the surface slow down until they have zero speed because of the no slip condition. It is possible to distinguish two regions in the fluid: the boundary layer region where viscous effects and velocity changes are significant, and the irrotational flow region where the velocity remains constant in the radial direction. The region called hydrodynamic entrance region is the region needed for velocity to develop completely; after this region with a specific length called entry length, the flow is said fully developed and the velocity profile does not change.

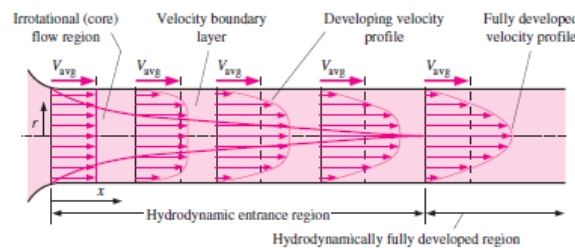


Figure 4.1 – The development of velocity [11].

The addition of the flow extensions is useful to have, at the real inlet and outlets of the models, a fully developed velocity profile. In general, flow extensions were added to a model to minimize the impact of boundary conditions applied to the model.

The first step was calculating the entry length for the models with circular section area: starting from the geometry of models, the flow rate is obtained with *Van del Giessen's* formula (4.1) [75], then the velocity and Reynold's number are calculated.

$$q = 1.43 * d^{2.55} \quad (4.1)$$

The entry length is calculated with following formula where  $d$  is the hydraulic radius.

$$L_h = 0.05 * Re * d \quad (4.2)$$

To obtain the length of inlet flow extensions of physiological models the procedure starts from the Reynold's number: it is one for the two right models and one for the two left models. From Reynold's number and using *Mimics* and *SimVascular* to obtain geometric parameters, the velocity and the flow rate are calculated. The entry length is calculated using formula (4.2).

Surface	Area [cm <sup>2</sup> ]	Velocity [cm <sup>2</sup> ]	Flow Rate [cm <sup>3</sup> /s]	Reynolds	Lh [cm]
LCA_Circ_Inlet	0,0593943	7,110108858	0,422299939	51,8142919	0,7124379
LCA_TC_Inlet	0,0861019	6,060365968	0,521809025	51,8142919	0,83584243
RCA_Circ_inlet	0,095755	8,108048527	0,77638943	75,02377449	1,30980188
RCA_TC_Inlet	0,119823	7,363426878	0,882307899	75,02377449	1,44225473

Table 4.1 – Inlet Flow extension lengths.

#### 4.1.2 STEADY SIMULATIONS

Since the relative low mesh sensitivity of flow rate, which is the only one parameter of interest in this first step, the mesh global edge size used is the value estimated by *SimVascular*.

The total hydraulic resistance value for each model is calculated as the ratio between the mean pressure (93 mmHg=123989,739 dynes/cm<sup>2</sup>) and the flow rate value at the inlet. The values are in table 4.2.

Model	R_tot [dyne*s/cm <sup>5</sup> ]
LCA_Circ	293605,87
LCA_TC	237615,17
RCA_Circ	159700,45
RCA_TC	140528,88

Table 4.2 – Total resistance values.

These values are used to set the boundary conditions. For each model, the total resistance value is subdivided through the outlets using the Murray's Law with the coefficient equal to 2.27 as showed in the paper of *Van der Giessen et al.* It is an

approximation because this coefficient is used to split a resistance between only two branches, while we have more branches.

Before running the simulation, it is necessary to set the solver parameters.

Parameters	Value
Timestep size	0.01 s
Number of Timesteps	200
Number of Timesteps Between restarts	10
Step Construction	5
<b>Advanced Parameters</b>	
Non-linear iteration control	
Residual Control	True
Residual Criteria	0.0001
Minimum Required Iterations	3
Linear solver	
Tolerance on Momentum Equation	0.01
Tolerance on Continuity Equation	0.1
Tolerance on svLS NS solver	0.1
Max N° of iterations for svLS NS solver	2
Max N° of iterations for svLS NS Momentum Loop	4
Max N° of iterations svLS NS Continuity Loop	400
Discretization Control	
Time Integration Rule	First Order
Time Integration Rho Infinity	0.5
Flow Advection Form	Convective
Quadrature Rule on Interior	2
Quadrature Rule on Boundary	3

Table 4.3 – Solver parameters.

At the end of simulations, the results are exported and the files .txt with the flow rates at each outlet are used in a Matlab code to calculate velocities, Reynolds numbers and primarily flow extensions length.

Cap	Lh [cm]
RCA_Inlet	1,44225473
RCA_1	0,483130072
RCA_2	0,325759916
RCA_3	0,448874261

Table 4.4 – Flow extension values of right coronary model obtained from TC images.

Cap	Lh [cm]
RCA_Inlet	1,309801885
RCA_1	0,405915897
RCA_2	0,371781968
RCA_3	0,53358283

Table 4.5 – Flow extension values of right coronary model with circular section area.



Cap	Lh [cm]
LCA_Inlet	0,835842432
LCA_1	0,153990284
LCA_2	0,076475957
LCA_3	0,186287686
LCA_4	0,200201084
LCA_5	0,128559581
LCA_6	0,089346256

Table 4.6 – Flow extension values of left coronary model obtained from TC images.

Cap	Lh [cm]
LCA_Inlet	0,712437901
LCA_1	0,222942573
LCA_2	0,082999112
LCA_3	0,139749531
LCA_4	0,156083476
LCA_5	0,100281174
LCA_6	0,056504111

Table 4.7 – Flow extension values of left coronary model with circular section area.

To add the flow extensions to the models have been used VMTK, in particular the script *vmtkflowextensions* that needs as input the surface, the centerlines, the extension mode and the extension length. This function adds to each surface cap a cylindrical pipe with the calculated length.

## 4.2 MESH SENSITIVITY ANALYSIS

The aim of this step is to find the element dimension which ensure the best compromise between results accuracy and computational costs. For this study simulations were performed only on right coronary model with circular section. Six meshes have been created and the mesh with twelve millions of elements is reference.

Mash name	Number of elements	Max edge size
RCA_2M	2017944	0,02400
RCA_4M	4061462	0,0188
RCA_6M	6165975	0,0163
RCA_8M	8028185	0,0148
RCA_10M	10060858	0,0137
RCA_12M	12045721	0,0129

Table 4.8 – Mesh parameters

The boundary conditions were imposed with the splitting of total resistance, using 2.27 as coefficient. The setting of the steady simulations was the same used to the one used for the previous simulations; only the timestep is changed. For 12M, 10M and 8M meshes  $\Delta t=0.0025$  s, while, for 6M, 4M and 2M  $\Delta t=0.005$  s, this because of convergence

issues during the simulations. For the results analysis we considered the same temporal instant for all meshes.

WSS [Dyne/cm <sup>2</sup> ]		MESH				
Statistical values	12 M	10 M	8 M	6 M	4 M	2 M
Mean	11,54020698	11,60770359	11,6842509	11,45880653	11,48064281	11,40206664
Standard Deviation	11,2022751	11,24063129	11,2558442	11,06519251	11,01557077	10,85729778
Skewness	2,742577252	2,695992092	2,644654243	2,7157723	2,656467006	2,621650253
Kurtosis	9,011061472	8,654478538	8,260599901	8,737265914	8,242437763	7,880891266

VELOCITY [cm/s]		MESH				
Statistical Values	12 M	10 M	8 M	6 M	4 M	2 M
Mean	7,717733634	7,7383468	7,743459311	7,642176655	7,658742911	7,679871284
Standard Deviation	5,625251484	5,620798933	5,617830533	5,611814664	5,608207962	5,622511282
Skewness	1,218574546	1,225954227	1,236256673	1,259771485	1,265947732	1,309235607
Kurtosis	2,727291786	2,759244103	2,804645829	2,889687366	2,904203564	3,041114753

WALL PRESSURE [Dyne/cm <sup>2</sup> ]		MESH				
Statistical values	12 M	10 M	8 M	6 M	4 M	2 M
Mean	126299,994	126275,0485	126305,807	126223,5418	126259,2549	126350,6288
Standard Deviation	771,8818946	782,8197844	789,447380	770,5542662	779,6046779	780,4770474
Skewness	-1,674205922	-1,668991901	-1,668223766	-1,669817426	-1,673120629	-1,669738632
Kurtosis	3,02140296	2,950822076	2,915347357	3,003798886	2,983344974	2,978537551

Table 4.9 – Statistical values obtained from simulations results.

Starting from these values, the percentage differences between 12M and other meshes have been evaluated.

WSS		PERCENTAGE DIFFERENCE			
Statistical values	12M/10M (%)	12M/8M (%)	12M/6M (%)	12M/4M (%)	12M/2M (%)
Mean	0,5848822	1,248191848	0,705363793	0,516144671	1,197035182
Standard Deviation	0,342396488	0,478198454	1,223703055	1,666664342	3,079529064
Skewness	1,698590641	3,57047406	0,977363632	3,139756444	4,409246792
Kurtosis	3,957169033	8,328226072	3,038438459	8,529779882	12,54203192

VELOCITY		PERCENTAGE DIFFERENCE			
Statistical Values	12M/10M (%)	12M/8M (%)	12M/6M (%)	12M/4M (%)	12M/2M (%)
Mean	0,267088326	0,333332011	0,979004758	0,764352934	0,490588978
Standard Deviation	0,079152921	0,131922117	0,238866122	0,302982404	0,048712524
Skewness	0,605599427	1,451050101	3,380748381	3,887590319	7,439927393
Kurtosis	1,171576782	2,836295088	5,954463001	6,486719866	11,50676172

WALL PRESSURE		PERCENTAGE DIFFERENCE			
Statistical Values	12M/10M (%)	12M/8M (%)	12M/6M (%)	12M/4M (%)	12M/2M (%)
Mean	0,019750977	0,004602533	0,060532196	0,032255815	0,040090887
Standard Deviation	1,417041895	2,275670106	0,171998903	1,000513598	1,113532124
Skewness	0,311432479	0,357313071	0,262124029	0,064824354	0,266830414
Kurtosis	2,336030157	3,510144272	0,582645707	1,259613076	1,418725332

Table 4.10 – Percentage differences.

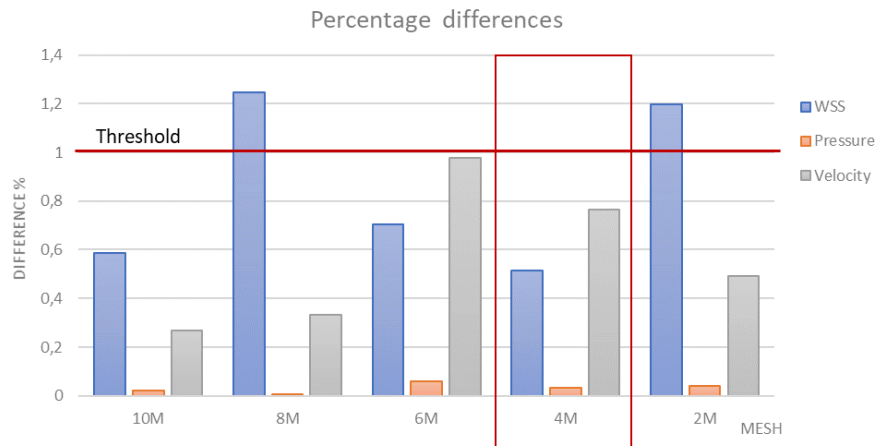


Figure 4.2 – Graphic of percentage differences based on mean values.

The objective is to find a mesh element size that gives results near the results of 12M mesh, but with a lower computational time. The 10M gives good results but the computational cost is too high. Among other meshes, the 4M mesh gives the best results in term of WSS and good results in term of velocity and pressure, all percentage difference were found lower than 1%.

To deepen the analysis, also the Probability Density Function (PDF) were evaluated; it represents the distribution of values assumed by a quantity. The area under the density function is the probability of the variable falling in a specific range of values.

In our analysis, the PDFs have been calculated using a Matlab script. The PDF values have been normalized relatively to the number of elements in order to have curves that can be compared with each other.

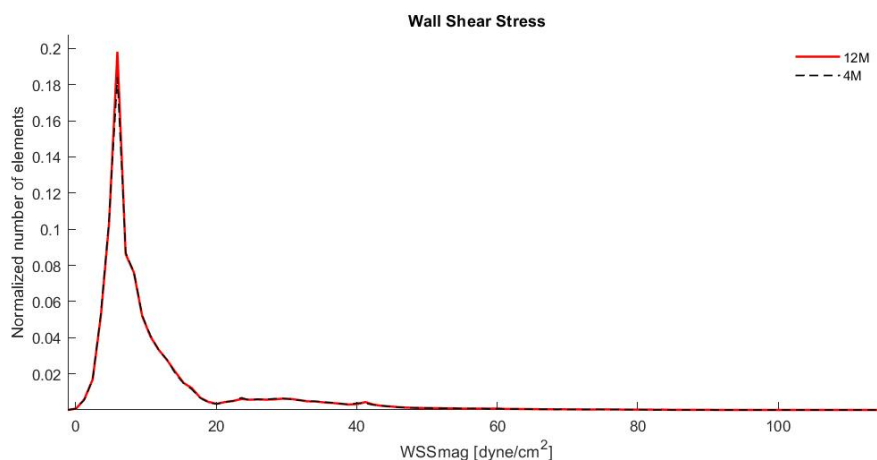


Figure 4.3 – PDF for WSS values.

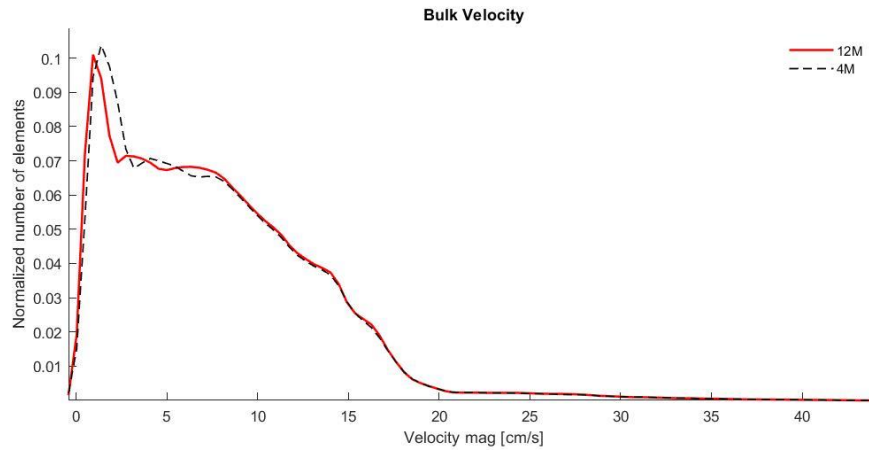


Figure 4.4 – PDF for Velocity values.

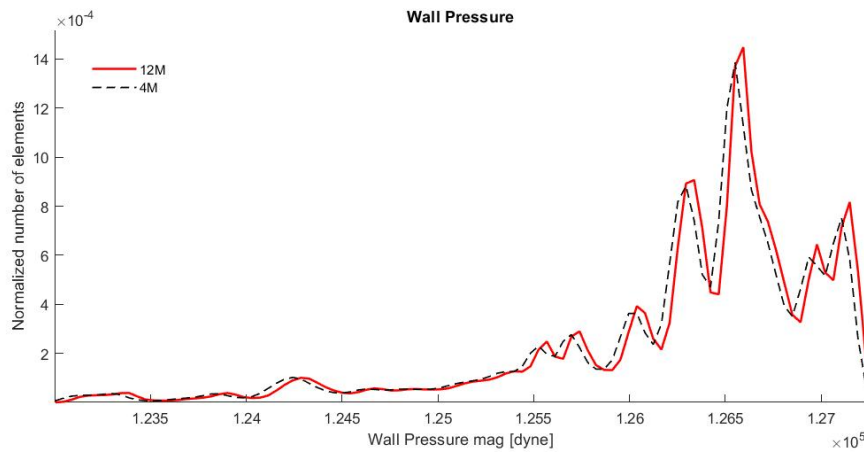


Figure 4.5 – PDF for Pressure values.

In conclusion, the element size chosen for the final meshes is 0.0188 cm; this value has been used for all models because they have similar dimensions and fluid dynamic conditions. The final meshes have two boundary layers, the portion of edge size and the layers decreasing ratio equal 0.8.

### 4.3 THE BOUNDARY CONDITIONS

#### 4.3.1 THE INLET VELOCITY WAVEFORMS

The waveforms used for the unsteady simulations were found in literature [72]. The digitalization of the images has been performed by a web application <https://automeris.io/WebPlotDigitizer/>. It requires to click four known points on the axis and to then assign a value to each of these points; the objective is the calibration of

axis. The algorithm returns a file with the X and Y values for each point on the curve. In our case, X and Y correspond to the time and the velocity. The next step is to rescale the time in order to have the starting point at zero and the flow rate is normalized relatively to the mean flow rate values found in literature [83] ( $Q_{LCA}=0.985$  ml/s,  $Q_{RCA}=0.64$  ml/s). Since we want a period of 1 s, we reconstructed the waveforms using the Fourier series with ten coefficients for the flow. The choice of the coefficients number (N) is given by a compromise between the accuracy of the curve reconstruction and the oscillations in the part of the curve obtained for interpolation.

If N is high, the reconstruction is true to reality, but the trend of the final part of the curve is very oscillatory; if N is low, the reconstruction is not so accurate. In our case, for both models, N equals 9.

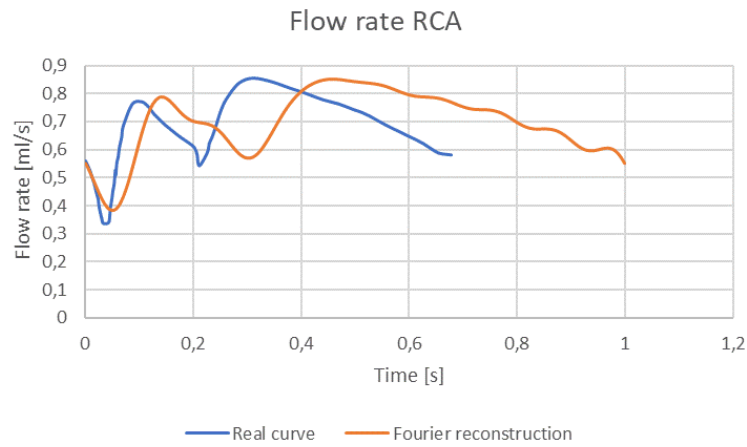


Figure 4.6 –Inlet flow rate curves for right coronary models.

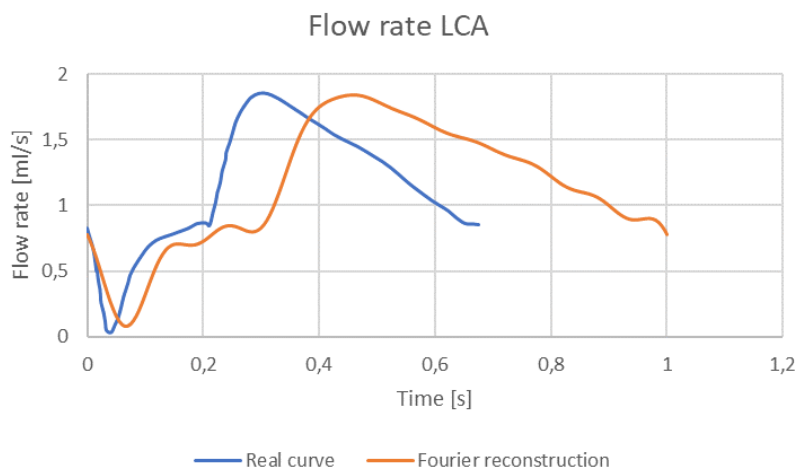


Figure 4.7 – Inlet flow rate curves for left coronary models.

### 4.3.2 RESISTANCES SIZING

During first stages we imposed the resistance splitting grouping all the outlets, in this final step resistances values were determined by applying the Van der Giessen flow split at each bifurcation.

Centrelines were divided into groups, and each group has an Id numbers: a name is assigned at each outlet showed in figure 4.8.

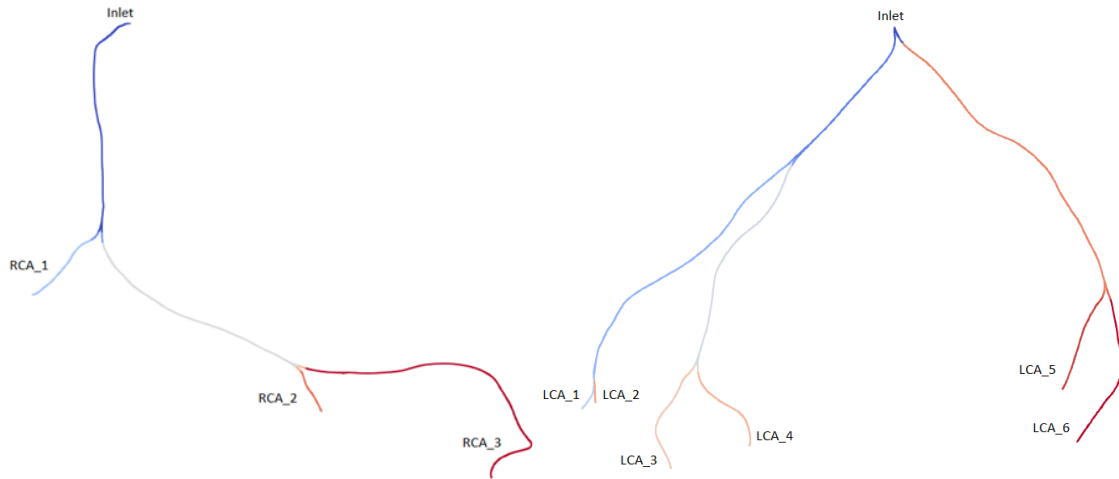


Figure 4.8 – The branches' names.

Starting from the mean diameters of each branch and from the inlet flow rates given by the literature, we calculated the flow ratio at each bifurcation using the following formula, where i-branch is the smallest one.

$$Ratio_{i,j} = \left( \frac{d_{Di}}{d_{Dj}} \right)^{2.27} \quad (4.3)$$

$$q_j = \frac{1}{1 + Ratio_{i,j}} \quad (4.4)$$

$$q_i = 1 - q_j \quad (4.5)$$

The results of these formula are non-dimensional and, multiplied by 100, represent the portion of flow in each branch. We obtain the real flow rates multiplying the inlet flow rates by the split coefficients,  $q_i$  and  $q_j$ . The resistance values are calculated as the ratio between the pressure (93 mmHg) and the flow rates obtained.

The results are showed in the tables 4.11 and 4.12.

RCA					
Branch	D_mean [cm]	Flow Split %	Flow Split	Flow Rate [ml/s]	Resistance [Dyne-s/cm <sup>5</sup> ]
RCA_1	0,153564391	16,73150757	0,167315076	0,107081648	1157899,05
RCA_2	0,167456938	37,67610901	0,376761090	0,241127098	514209,0632
RCA_3	0,182133771	45,59238342	0,455923834	0,291791254	424926,1667

Table 4.11 – Resistance values for right coronary model.

LCA					
Branch	D_mean [cm]	Flow Split %	Flow Split	Flow Rate [ml/s]	Resistance [Dyne-s/cm <sup>5</sup> ]
LCA_1	0,191507877	13,25429349	0,132542935	0,130554791	949714,2015
LCA_2	0,168355069	9,892962756	0,098929628	0,097445683	1272398,479
LCA_3	0,138209755	10,12031482	0,101203148	0,099685101	1243814,149
LCA_4	0,132438629	9,186381827	0,091863818	0,090485861	1370266,444
LCA_5	0,146686787	25,31144262	0,253114426	0,24931771	497316,2118
LCA_6	0,163173227	32,23460448	0,322346045	0,317510854	390505,5131

Table 4.12 – Resistance values for left coronary model.

#### 4.4 THE SETTING OF FINAL SIMULATIONS

The final simulations are unsteady, the flow rate waveforms are showed in figure 4.12.

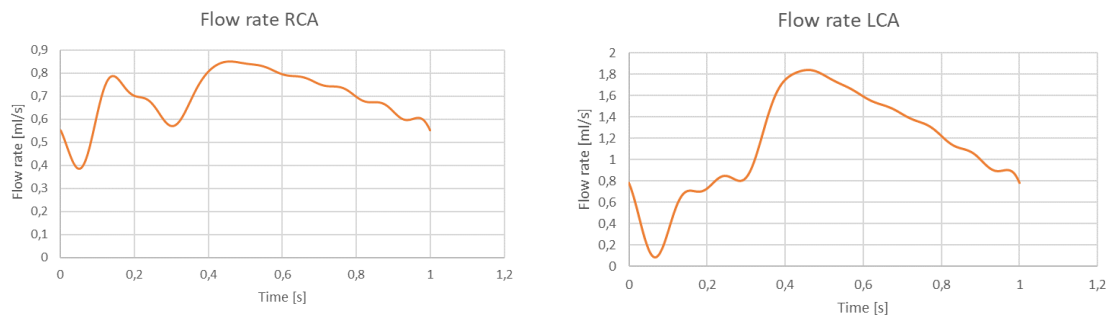


Figure 4.9 – Final flow rate waveforms.

The boundary conditions are the resistance values contained in the tables 4.11 and 4.12. About the solver parameters, we have been chosen to simulate two cardiac cycles. The first one is useful to extinguish the transient behaviour that originates from the starting condition.

Parameters	Value
Timestep size	0.005 s
Period	1 s
<b>Advanced Parameters</b>	
Non-linear iteration control	
Residual Control	True
Residual Criteria	0.0001
Minimum Required Iterations	3
Linear solver	
Tolerance on Momentum Equation	0.01
Tolerance on Continuity Equation	0.1
Tolerance on svLS NS solver	0.1
Max N° of iterations for svLS NS solver	5
Max N° of iterations for svLS NS Momentum Loop	10
Max N° of iterations svLS NS Continuity Loop	400
Discretization Control	
Time Integration Rule	Second Order
Time Integration Rho Infinity	0.5
Flow Advection Form	Convective
Quadrature Rule on Interior	2
Quadrature Rule on Boundary	3

*Table 4.13 – The solver parameters in the final simulations.*



# 5 RESULTS

After the unsteady-state fluid dynamic simulations, only the second cardiac-cycle was considered for data analysis, in order to avoid the impact of initial conditions. For each time-step wall and volume data have been exported from *SimVascular*, in particular, for wall data WSS and pressure data, while for volume pressure and velocity data. Other informations regarding pressure and flow rate at boundaries were exported in terms of surface averaged values for each time-step.

To exclude flow extensions from data analysis, wall and volume data were projected on the correspondent model surface and volume mesh without flow extensions. To do this, the VMTK scripts *vmtksurfaceprojection* and *vmtkvolumeprojection* have been used. The output files have been used as input files of a Python script for the surface descriptors calculation.

## 5.1 SURFACE DESCRIPTORS ANALYSIS

The TAWSS, expressed by the formula 2.12, is the Time-Averaged Wall Shear Stress and it is the integration of each nodal WSS over the cardiac cycle. It has been calculated as the summation of WSS absolute values at each point of the surface multiplied by the inverse of period and the size of timestep (0.005 s). The OSI and RRT calculation followed the formulas 2.13 and 2.14, indicate respectively the extent of the WSS oscillation during the cardiac cycle and the permanence time of the fluid particle near the wall. The descriptors have been saved in a single file *.vtp* for each model.

### 5.1.1 TAWSS ANALYSIS

For the TAWSS visualization the open source software *ParaView 5.6.0* has been used. It was decided to show the TAWSS in a range between 0 and 1.8 Pa, highlighting the low values in red to indicate their potential atheroprone effect [35].

The colour maps obtained for the TAWSS are showed in the following figures.

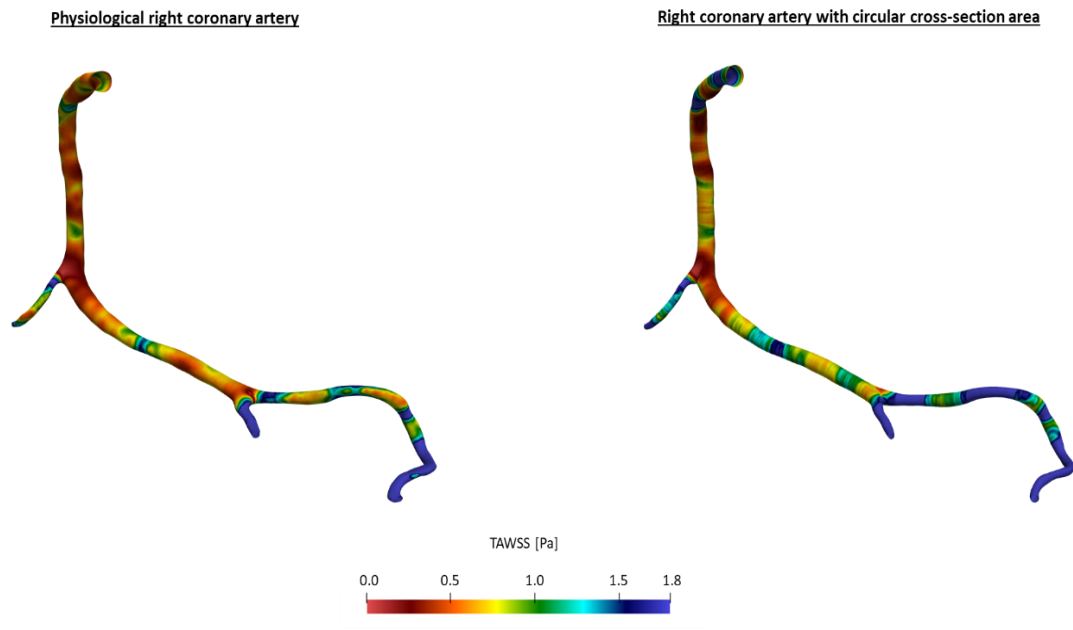


Figure 5.1 – TAWSS representation in right coronary models.

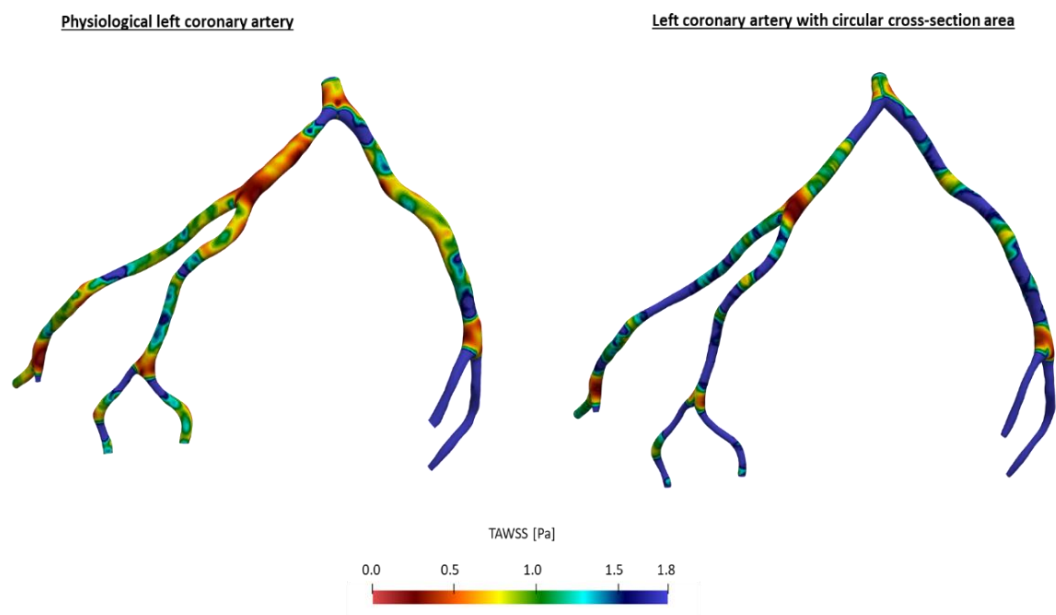


Figure 5.2 – TAWSS representation in left coronary models (first view).

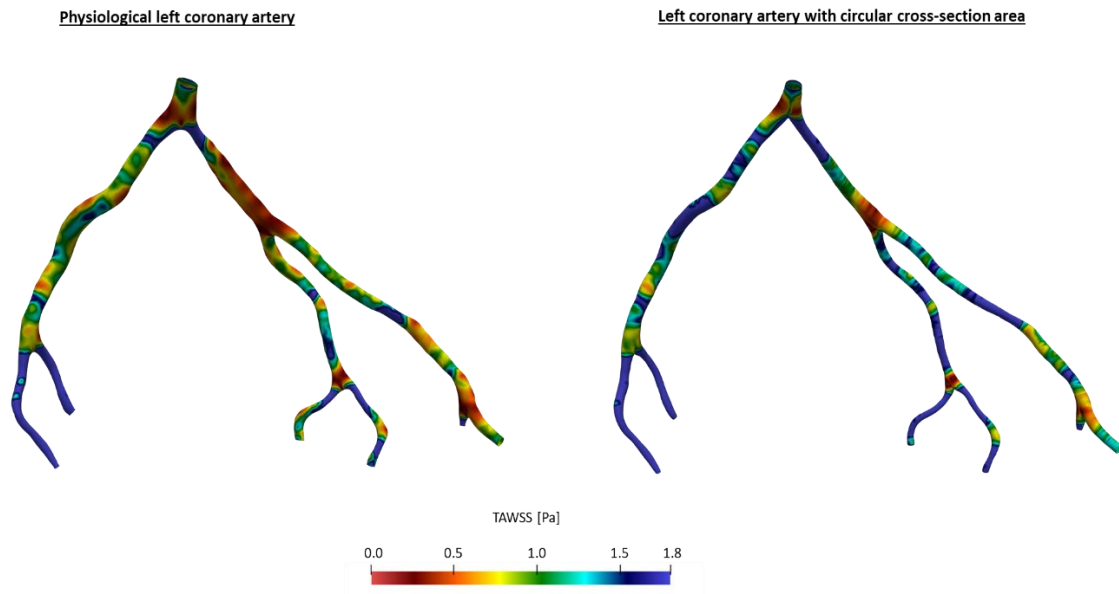


Figure 5.3 – TAWSS representation in left coronary models (second view).

It is possible to notice that the circular cross-sectional area models overestimate the TAWSS values: some low TAWSS areas in CT-based models, have not been recognized as such in the models with circular cross-section. These lacks have negative consequences with regard to the identification of atherogenesis risk areas.

### 5.1.2 OSI ANALYSIS

The OSI values are aligned to the OSI values showed in the study of *De Nisco et al.* [80]: in healthy coronary arteries this descriptor has very low values. Our results show slightly higher values in correspondence of bifurcation in the right coronary models; instead, in the left coronary models, the colour maps highlight larger areas with slightly higher OSI values.

The threshold value chosen to display significant OSI variations is 0.005.

Physiological right coronary artery

Right coronary artery with circular cross-section area

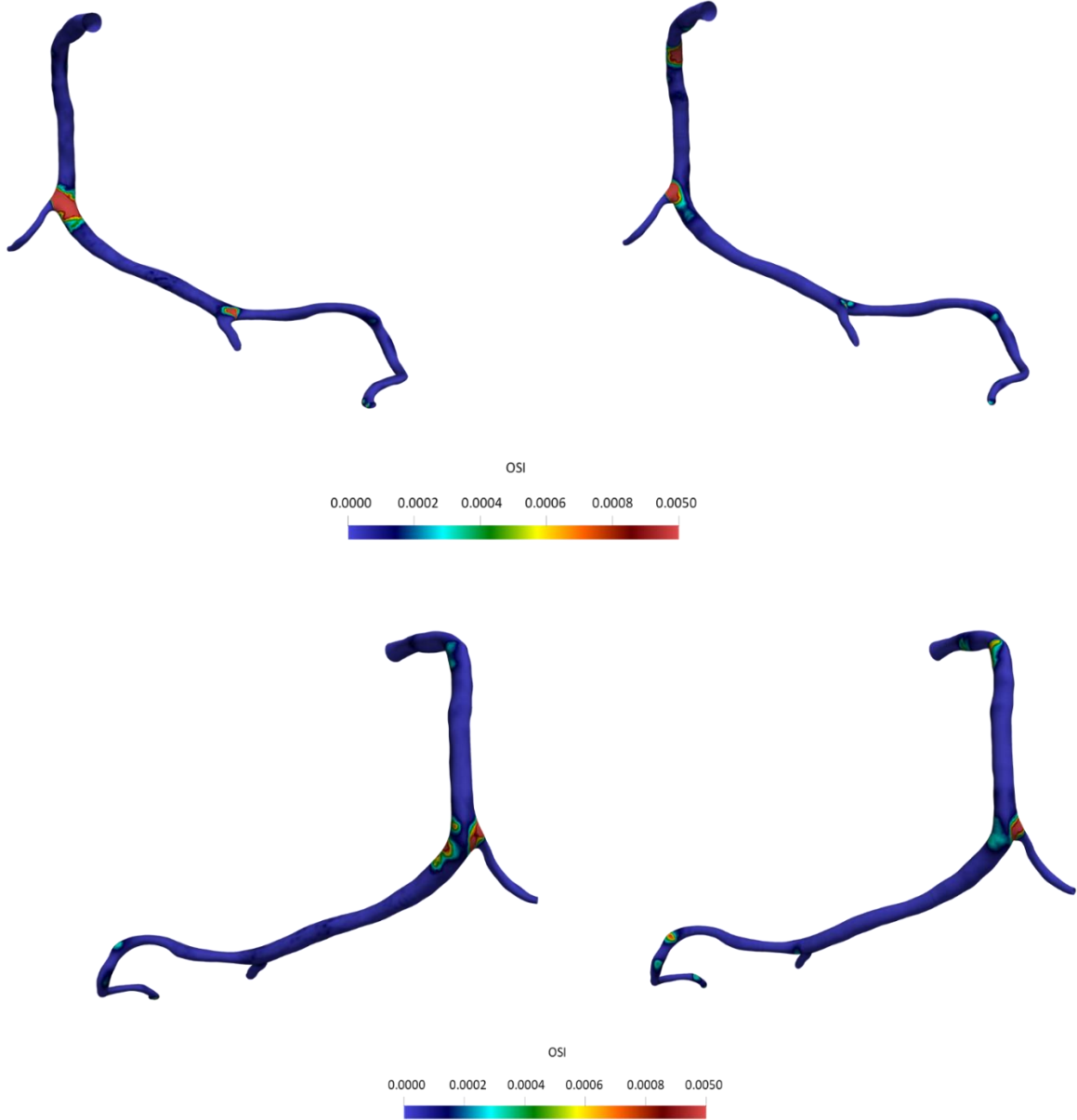


*Figure 5.4 – OSI representations in right coronary models.*

Physiological left coronary artery

Left coronary artery with circular cross-section area

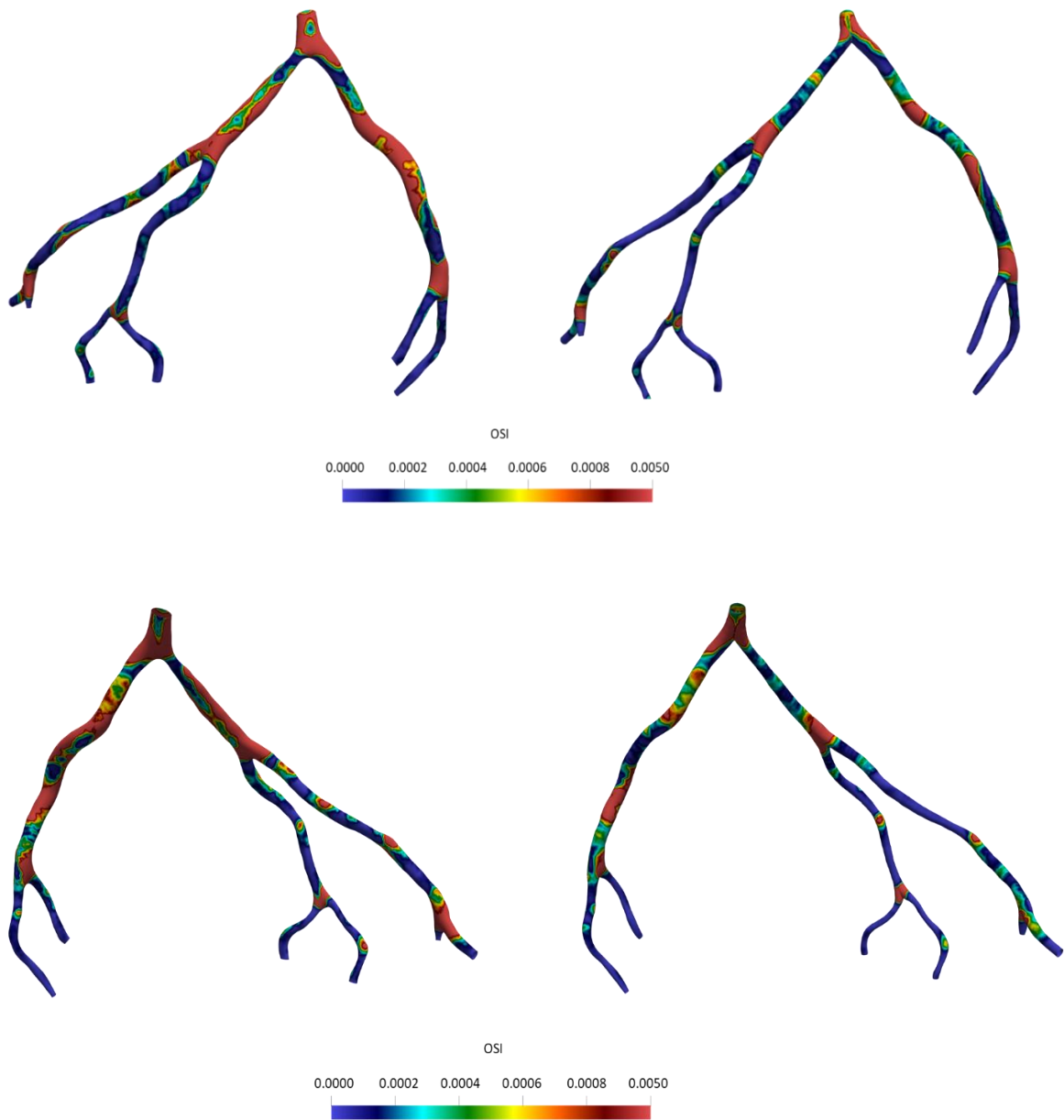


*Figure 5.5 – OSI representations in left coronary models.*

### 5.1.3 RRT ANALYSIS

From the RRT analysis is possible to notice that, as expected, this parameter is almost completely influenced by TAWSS values because the OSI values are small compared to TAWSS. Also, RRT values are very low; for a significative representation, the range chosen is from 0 to 5  $\text{Pa}^{-1}$ . The lowest RRT areas are located in correspondence of bifurcations and curvatures, where TAWSS values are lower.

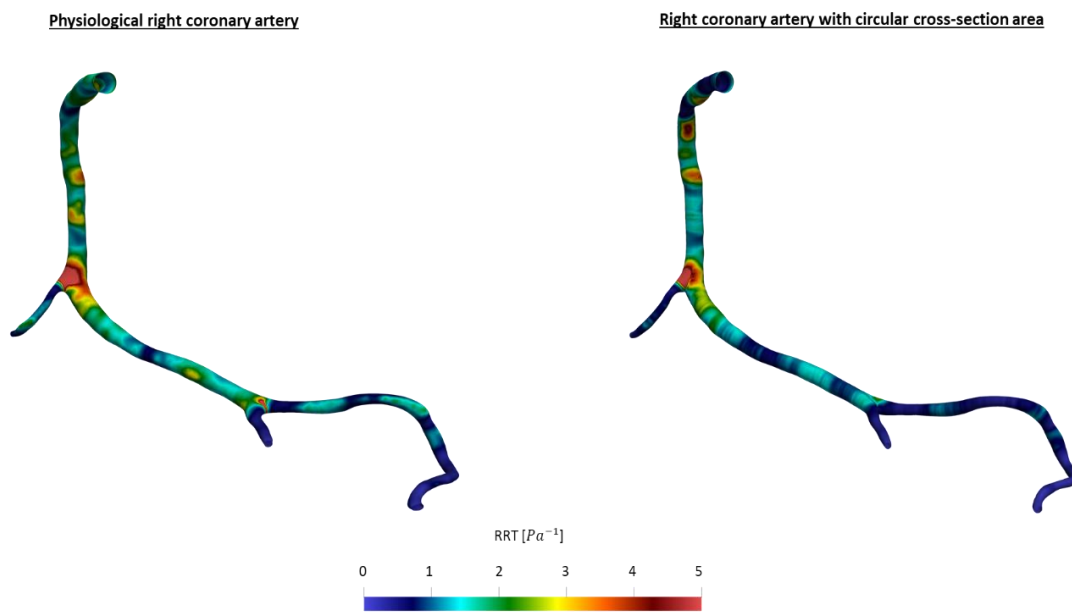


Figure 5.6 – RRT representation in right coronary models.

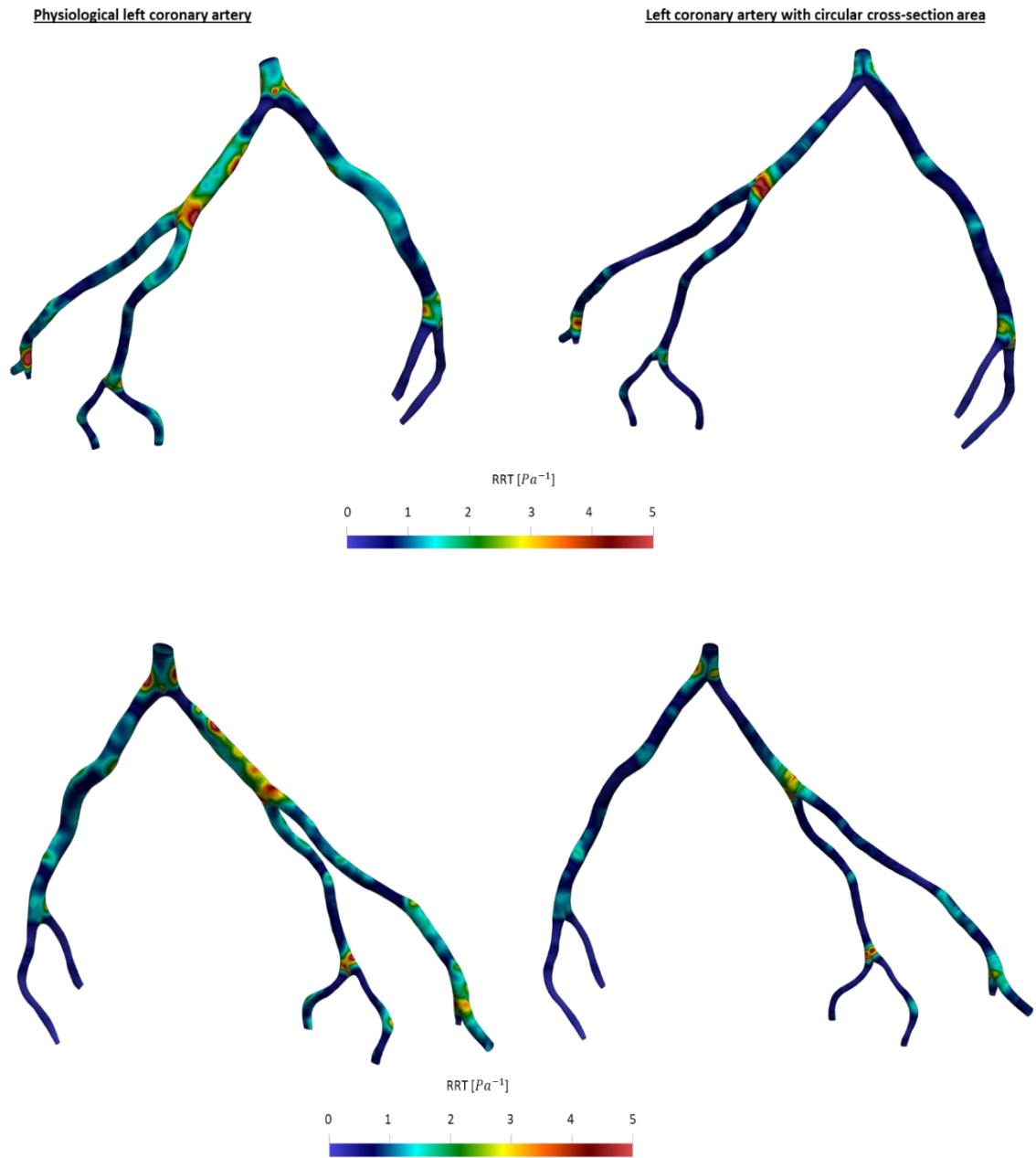


Figure 5.7 – RRT representations in left coronary models.

#### 5.1.4 CORRESPONDANCES BETWEEN GEOMETRY DISTANCE AND SURFACE DESCRIPTORS DIFFERENCES

The difference between the model reconstructions are not so evident, but the VMTK function, *vmtksurfacedistance*, allows to calculate the pointwise minimum distance of an input surface from a reference surface.

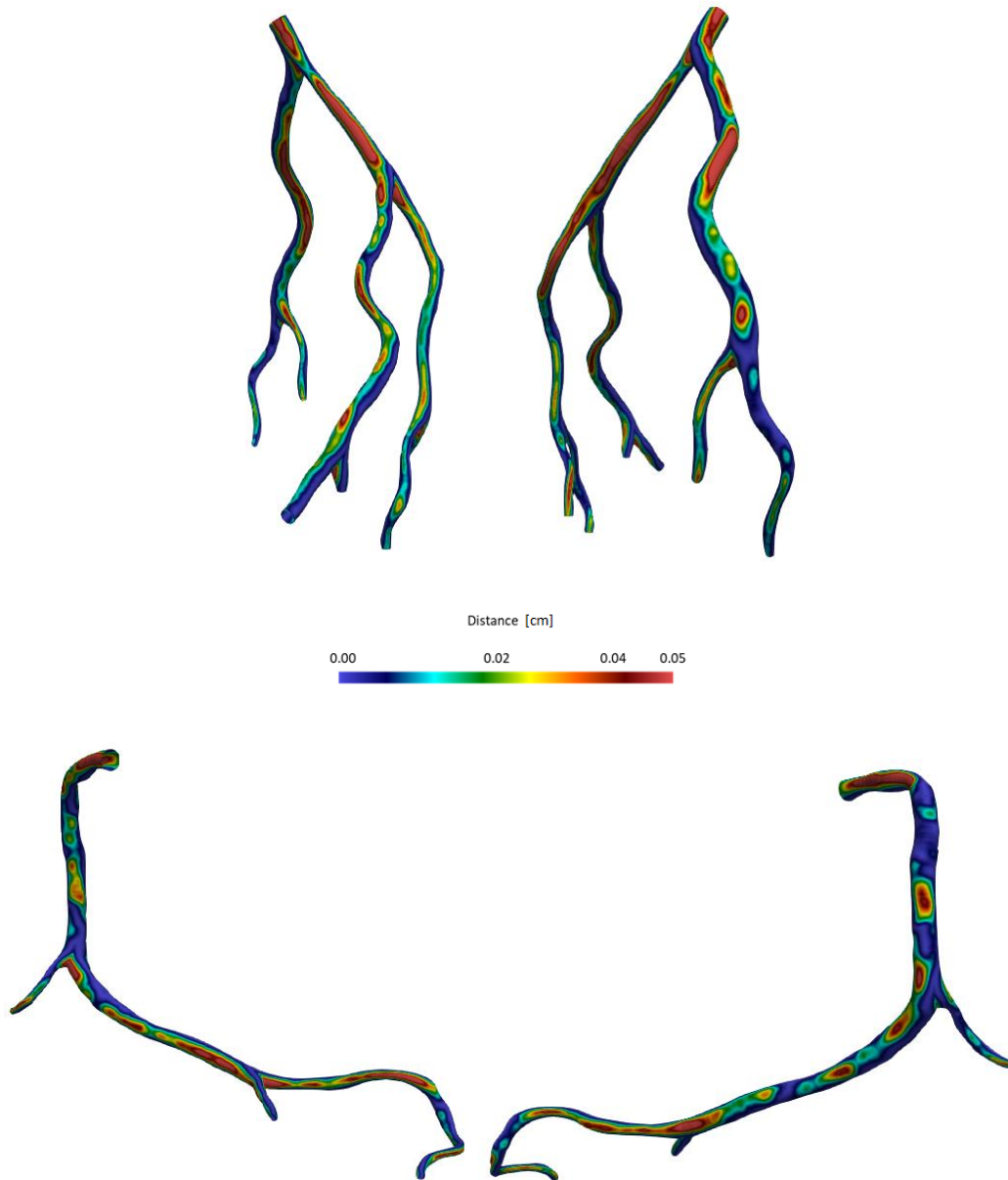


Figure 5.8 – Distance of circular model from physiological model for the left (top) and right (bottom) coronary.



Observing the colour maps of descriptors and the colour maps of the distance between the two reconstruction it is possible to note that the areas where the differences between the two reconstruction are most relevant have a correspondence with the areas where the geometrical distance is higher. The following figures show these correspondences.

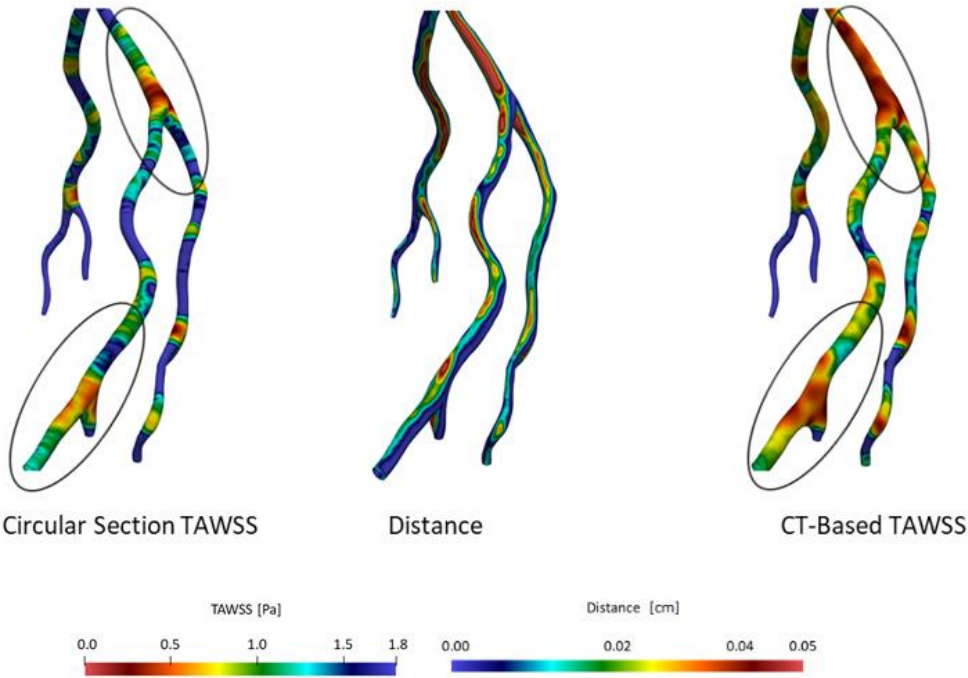


Figure 5.8 – TAWSS and geometry distance in left coronary artery (first view).

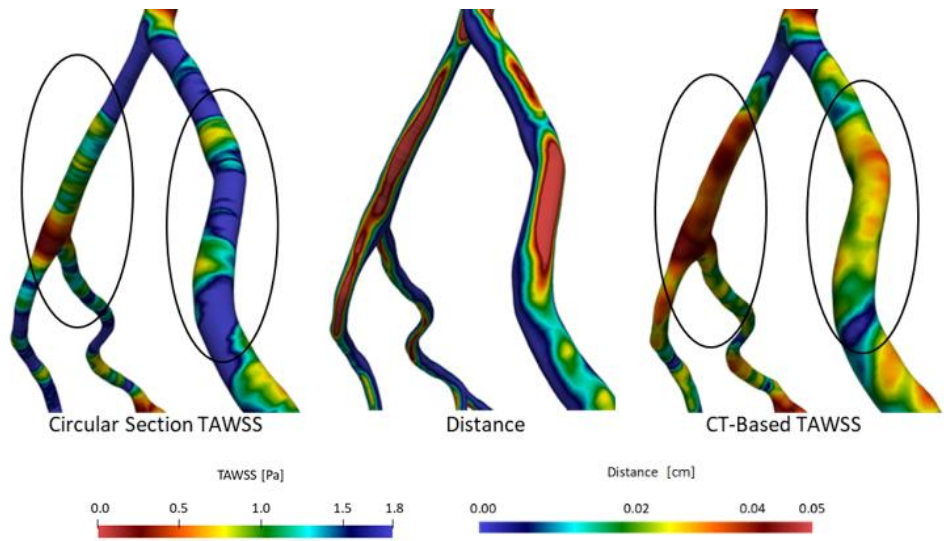


Figure 5.9 – TAWSS and geometry distance in left coronary artery (second view)

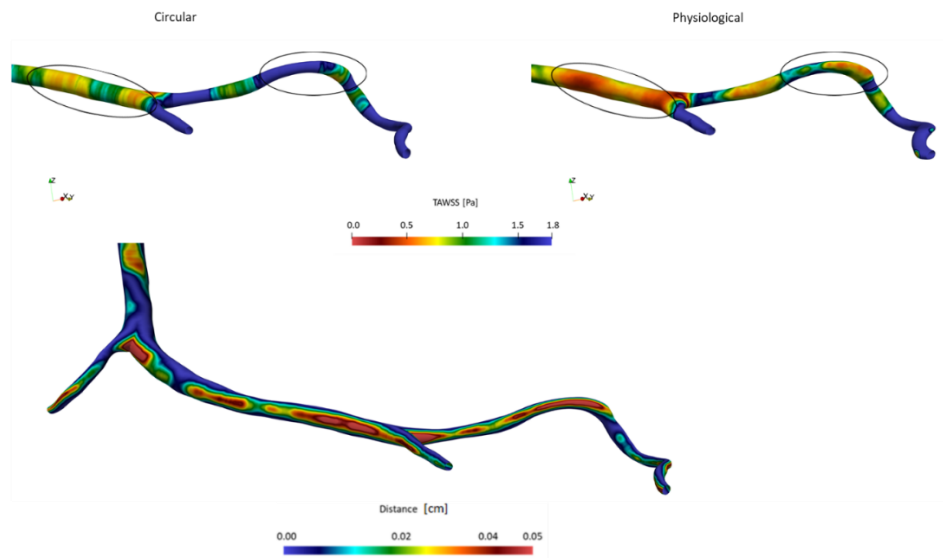


Figure 5.10 - TAWSS and geometry distance in right coronary

Observing the TAWSS distribution in left coronary artery models it is possible to note that the areas where the geometrical difference is higher have a correspondence with bifurcations and curvatures. The same consideration can be applied to the OSI.

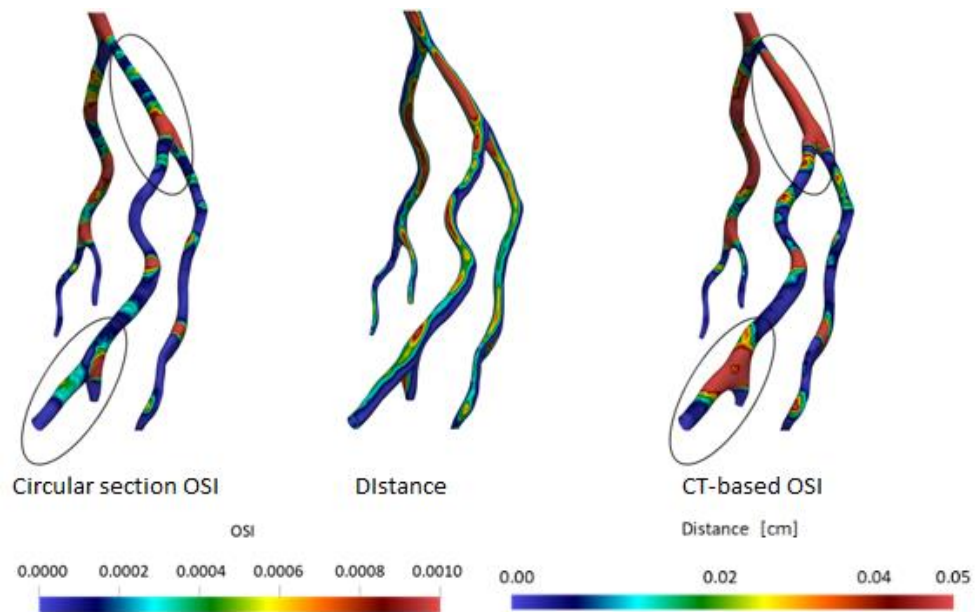


Figure 5.11 - OSI and geometry distance in left coronary artery.

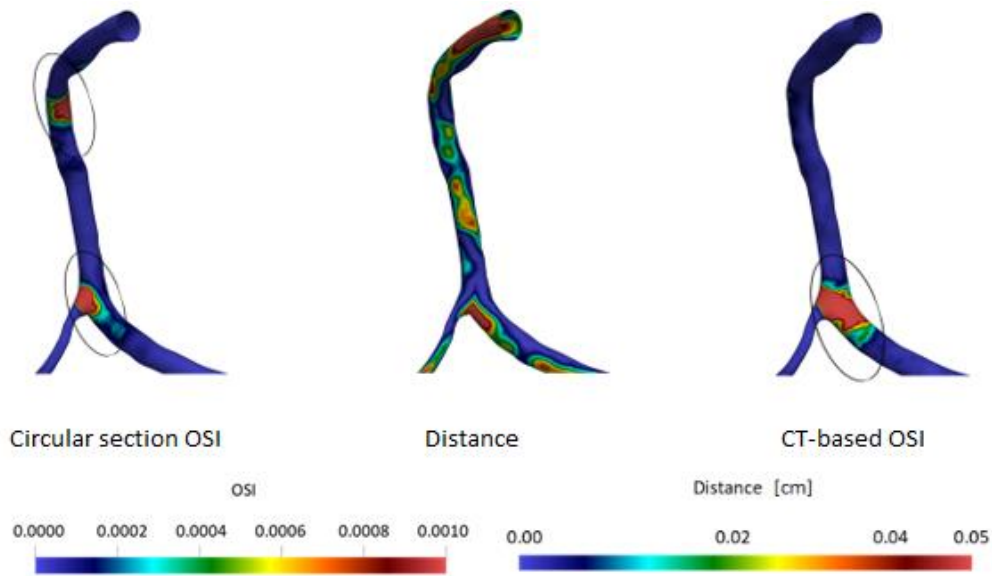


Figure 5.12 – OSI and geometry distance in right coronary artery.

#### 5.1.5 RISK-AREAS ANALYSIS

To define an objective threshold for the quantitative analysis of atherogenesis risk areas and differences between the models, it was necessary to obtain the percentiles for each descriptor. The population considered for the calculation includes all four models.

For the TAWSS the 10<sup>th</sup> and the 20<sup>th</sup> percentile have been used (TAWSS10 and TAWSS20 respectively) while for the OSI and the RRT, the 80<sup>th</sup> and the 90<sup>th</sup> percentiles have been used (OSI80, OSI90, RRT80 and RRT90 respectively).

Percentile values obtained are showed in the following table.

Descriptor	10th percentile	20th percentile	80th percentile	90th percentile
TAWSS [Pa]	0,462331381	0,601143953		
OSI			0,002524937	0,006225979
RRT [Pa <sup>-1</sup> ]			1,672015185	2,181252738

Table 5.1 – Percentiles values.

The visualization of areas TAWSS10, TAWSS20, OSI80, OSI90, RRT80 and RRT90 has been obtained imposing the appropriate colour scale in *Paraview*. The following figures show the atherogenesis risk areas.

Physiological right coronary artery

Right coronary artery with circular cross-section area



*Figure 5.13 – TAWSS risk areas for right coronary models.*

Physiological left coronary artery

Left coronary artery with circular cross-section area

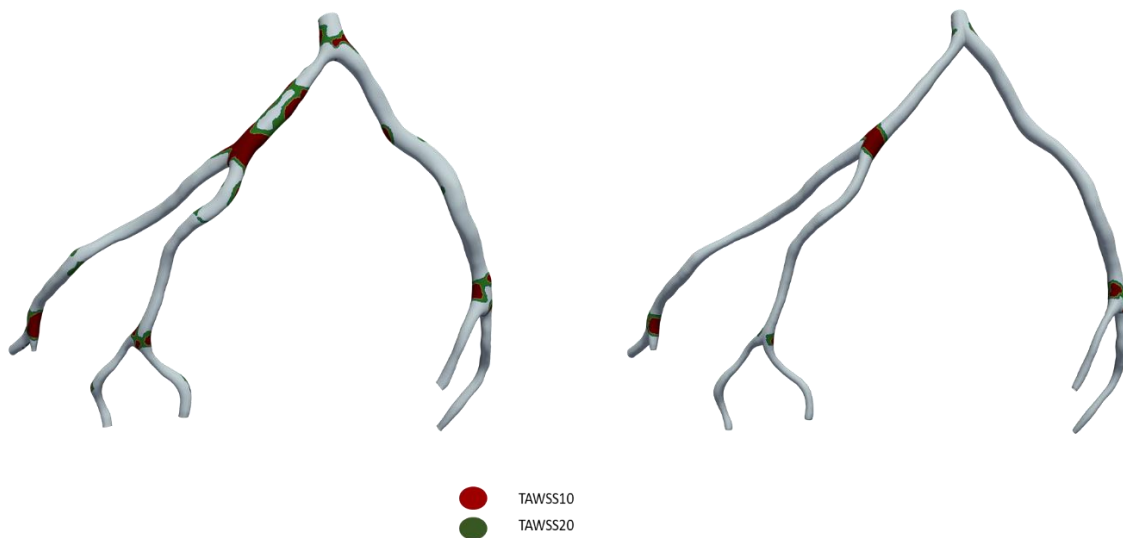


*Figure 5.14 – TAWSS risk areas for left coronary models.*

Physiological right coronary artery

Right coronary artery with circular cross-section area



*Figure 5.15 – RRT risk areas for right coronary models.*

Physiological left coronary artery

Left coronary artery with circular cross-section area

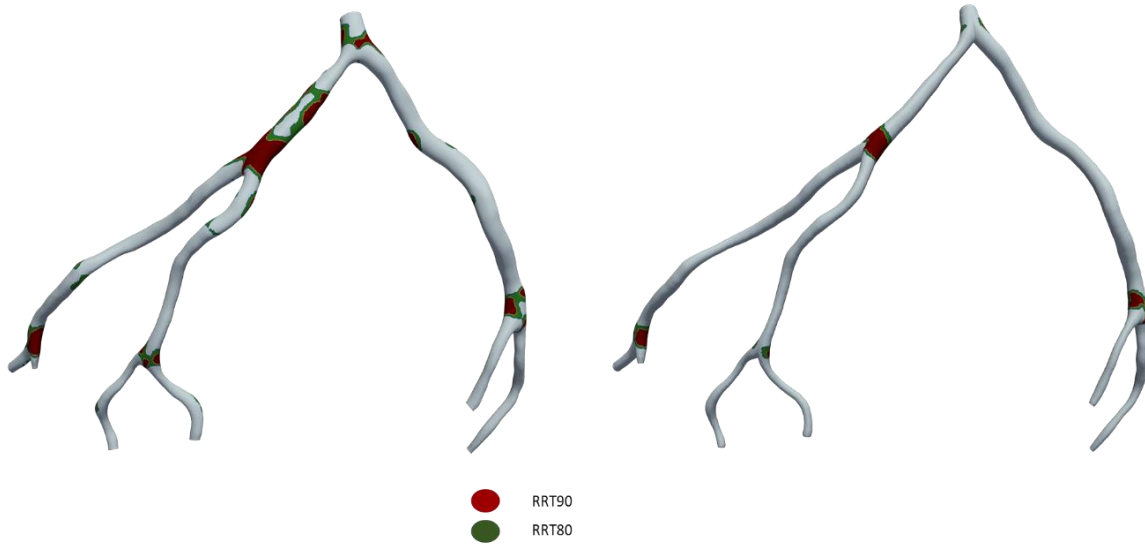


*Figure 5.16 – RRT risk areas for left coronary models.*

These are qualitative representations of the areas that are most at risk of atherogenesis, but they have to be quantified, in order to obtain appropriate conclusions.

The percentages of area subjected to low TAWSS values and high OSI and RRT values have been calculated using the following formula.

$$Area\% = \frac{Area\ of\ interest}{Total\ Area} * 100 \quad (5.1)$$

The percentages of areas have been compared in two histograms: one for the right and one for the left coronary.

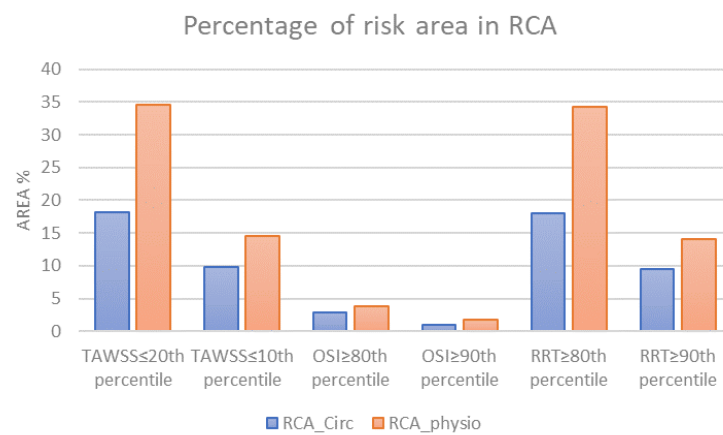


Figure 5.17 – Percentage of risk area in RCA.

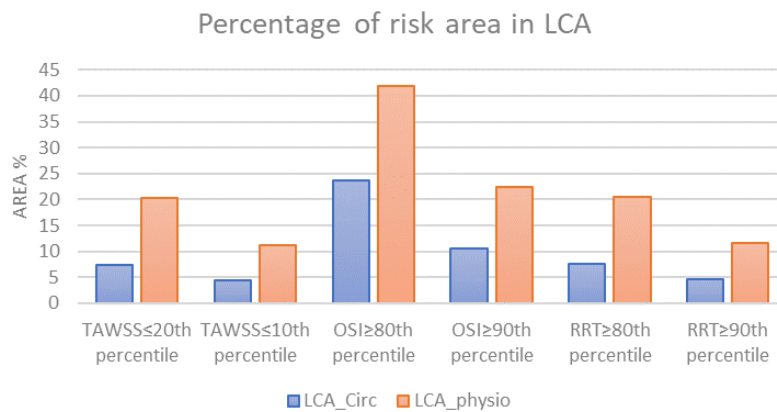


Figure 5.18 – Percentage of risk area in LCA.

Watching the graphs, it is possible to notice a general hemodynamic risk underestimation in the models with the circular cross-section area.

The TAWSS20 area is the 34.35 % of total area in the right CT-based model, while, in the right circular cross section model is only the 18.14%; the TAWSS10 area is respectively the 14.51% and the 9.79% of the total area. In both reconstruction of right coronary arteries, the OSI80 and OSI90 percentage areas are lower than 5%. Considering the RRT for the right coronary reconstructions, the RRT80 and RRT90 percentage areas are respectively the 34,19% and 14,10% of the total area in in the CT-based model; in the circular cross section reconstruction the percentages are the 18.09% and 9.57% of the total area.

In the left coronary reconstructions, the percentage areas subjected to high OSI values are more significant: the OSI80 area is the 41.83% of the total area in the CT-based model and the 23.62% in the circular cross-section reconstruction. Considering the TAWSS20 and the TAWSS10, the values obtained are respectively the 20.26% and the 11.29% of the total area in the CT-based model; in the circular cross-section reconstruction the percentages are the 7.43% and the 4.41% of the total area.

The underestimation of risk areas is a significative problem because potentially areas at risk of atherogenesis could not be recognised as dangerous analysing a model reconstructed with circular section area, this means neglecting significant criticality.

## ***5.2 BULK-FLOW DESCRIPTORS ANALYSIS***

First of all, the vorticity in the three directions has been obtained. The Jacobian matrix of velocities has been calculated and then, with Jacobian components, the curl of velocity has been obtained. Multiplying each component of velocity by the corresponding vorticity and by adding the results along the three direction, the helicity has been obtained. With the helicity, the LNH values for each timestep has been calculated and then averaged on the period.

As explained previously, LNH is always between -1 and 1 and for the representations the chosen threshold value is 0.2. the iso-surfaces with LNH values higher than 0.2 and lower than -0.2 have been visualized.

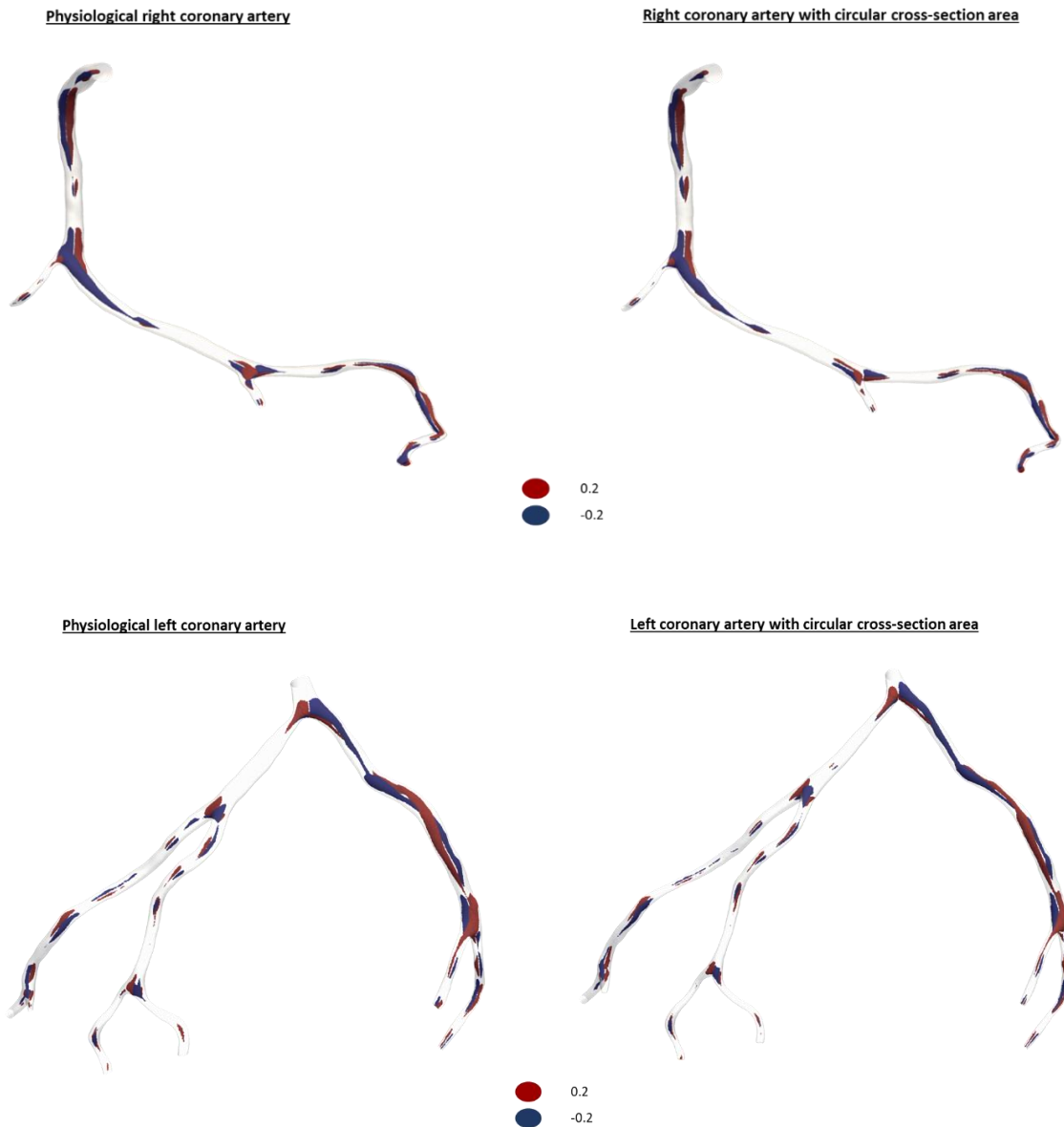


Figure 5.19 – LNH iso-surfaces.

Positive values of LNH indicate the presence of left-handed rotating structures, while negative values indicate right-handed rotating structures considering the forward fluid movement. From images acquired it is possible to observe how the rotating structures are well balanced: each left-handed rotating structure has almost always the corresponding right-handed rotating structure.



The last evaluation has been the calculation of four helical flow descriptors following formulas 2.20. The results obtained are showed in figure 5.20 and numerical values are in table 5.2.

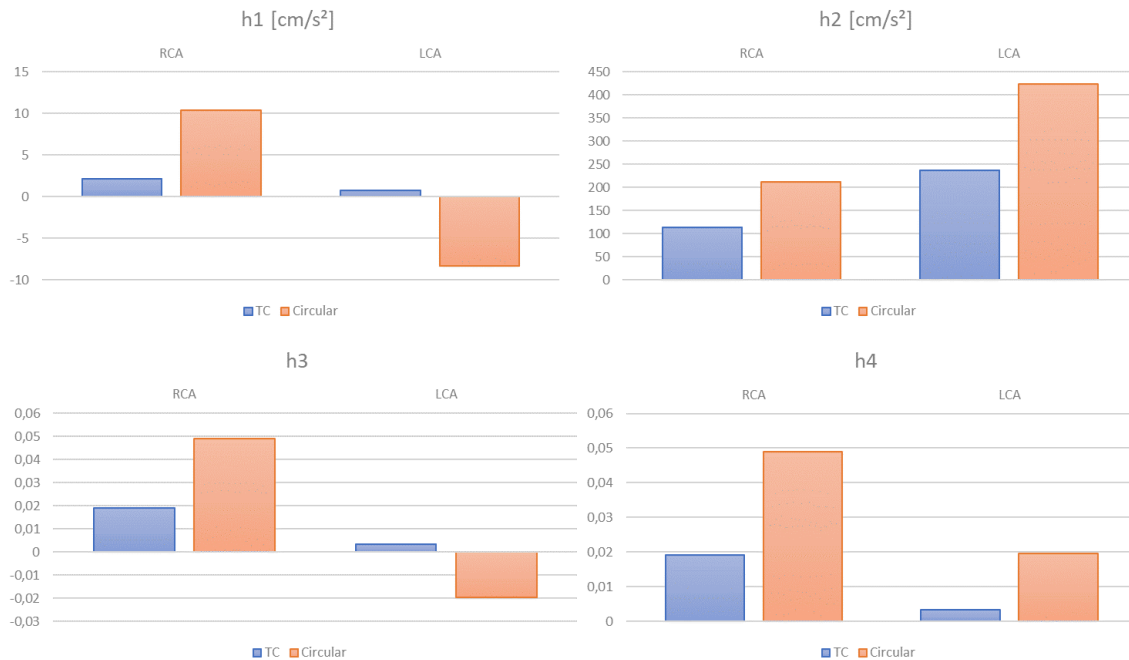


Figure 5.20 – Helical flow descriptors.

Model	$h_1$ [cm/s <sup>2</sup> ]	$h_2$ [cm/s <sup>2</sup> ]	$h_3$	$h_4$
RCA_circ	10,3670	211,6171	0,0490	0,0490
RCA_TC	2,1919	114,0324	0,0192	0,0192
LCA_circ	-8,2876	423,0896	-0,0196	0,0196
LCA_TC	0,8031	236,4052	0,0034	0,0034

Table 5.2 – Helical flow descriptors: numerical values.

Evaluating  $h_3$  and  $h_4$  it is possible to observe that the reconstruction with circular cross-section area does not significantly alter the symmetry of the flow structures, because the values are near zero. The time-averaged helicity normalized with the volume ( $h_1$ ) also has low values those indicate the good symmetry of the structures in both reconstructions.

Instead, the helicity intensity, represented by  $h_2$ , have high values and in the reconstruction with circular cross-section area these values are significantly higher than

values in the models TC-based. Consequently, the approximation of circular area leads to the overestimation of helicity intensity.

As previously stated, the presence of helical structures has beneficial atheroprotective effects on the low WSS areas [80]. The overestimation of the helicity intensity leads to the underestimation of haemodynamic risk and to neglect the atheroprone regions. This result is consistent with the result obtained from the analysis of TAWSS values: reconstructing models with circular cross-section area introduces a significant and dangerous underestimation of the atherogenesis risk.

# 6 CONCLUSIONS

Image-based computational simulations are a powerful tool for the study of atherogenic risk in coronary arteries.

Tomographic imaging is the gold standard for vessels three-dimensional reconstruction, despite this, also angiographic projections allow to reconstruct three-dimensional vessel models. Even if there is no information regarding the third dimension, it is still possible to reconstruct the model by starting from the centerlines obtained from the angiographic images and estimating the vessel section to a circular shape.

This thesis aims to evaluate the impact of approximation introduced by the circular cross-section area reconstruction on the main haemodynamic descriptors.

The first step was the reconstruction of two CT-based models: one for the left and one for right coronary arteries. The models with circular cross-section have been obtained starting from the centerlines extracted from the CT-based models. The reconstructions have been made on a reduced number of branches and the segments where the vessel diameter was inferior to 1 mm have been cut.

The final simulations are unsteady: physiological waveforms have been imposed to the inlets and to the outlets, hydraulic resistances, obtained from *Van der Giessen* flow splitting coefficient, have been imposed. The simulations are based on the Finite Element Method (FEM): the solver calculates the numerical solution of governing equations based on the volume discretization.

This study is based on the comparison between the results obtained from the unsteady simulations ran on CT-based models and the ones obtained from circular section ones. In order to obtain an analysis of the descriptors' differences between the two reconstructions that is not only qualitative, but also quantitative, a quantification of the most at risk atherogenesis areas has been made.

It can be noticed that in the case of circular section reconstruction TAWSS values are overestimated, while the OSI and RRT values are underestimated. This means that the area percentage that is the most at risk of atherogenesis (low TAWSS values and high OSI and RRT values) is underestimated. This can also be confirmed during the evaluation of the helicity, specifically of the helical flow descriptors ( $h_1$ ,  $h_2$ ,  $h_3$ ,  $h_4$ ).  $H_1$  has low values

for both reconstructions and this suggests a good symmetry of the helical flow structures. This is confirmed also from  $h_3$  and  $h_4$  values, which are very close to zero and this indicates that the left-handed and the right-handed rotating structures are well balanced. The assumption of a circular section doesn't significantly alter the structures' symmetry. On the other hand,  $h_2$  presents elevated values and the difference between the two types of reconstruction is considerable: the helicity intensity is overestimated in the circular section models. Since the helical structures have a positive impact on atheroprotection, their overestimation can cause an underestimation of the haemodynamic risk. Findings of helicity-based descriptors is perfectly coherent with what emerged during the analysis of the surface descriptors. In addition comparing the surface distribution of haemodynamic descriptors with the geometrical distance between the two reconstructions, it can be observed that exist a colocalization between areas with different values of hemodynamics descriptors and the areas in which the geometrical distance is bigger.

The qualitative and quantitative results' analysis leads to the conclusion that the error introduced by the circular section model is significant, but this study has some limitation. First of all, only two models have been considered: it can be interesting to conduct the study on a greater variety of models. Moreover, the circular section reconstructions have been obtained from centerlines extracted from CT-based models: another study could be conducted starting from angiographic images.

# BIBLIOGRAPHY

- [1] OpenStax, "16.3 Circulatory and Respiratory"
- [2] OpenStax, "Anatomy and Physiology.", OpenStax, 2013
- [3] T. Azuma, M. Hasegawa, "Distensibility of the vein: from the architectural point of view.", Biorheology 10, 1973, pp. 469-479.
- [4] F. Montevvecchi, A. Radaelli, "BIOMECCANICA. Analisi multiscala di tessuti biologici", collana di ingegneria biomedica, Pàtron Editore, 2007
- [5] P. Vennemann, R. Lindken, J. Westerweel, "In vivo whole-field blood velocity measurement techniques", Exp Fluids 42, 2007: pp 495-511.
- [6] S. S. Shibeshi, W. E. Collins, "The rheology of blood in branched arterial system", App Rheol. 2005, 15(6): pp 398-405.
- [7] B. M. Johntson, P. R. Johnston, S. Corney, D. Kilpatrick, "Non-Newtonian blood flow in human right coronary arteries: steady state simulations", Journal of Biomechanics 37, 2004: pp 709-720.
- [8] J. Boyd, J.M. Buick, S. Green, "Analysis of the Casson and Carreau-Yasuda non-Newtonian blood models in steady and oscillatory flows using the lattice Boltzmann method", Phys. Fluids 19, 2007.
- [9] "turbulent flow" [online] available:  
<https://www.cvphysiology.com/Hemodynamics/H007>
- [10] H. Kundela, "turbulent flow"
- [11] P. M. Page, "Flow in pipes," UioUniversitet i Oslo, pp. 321–343, 2004.
- [12] R. A. Cassanova, D. P. Giddens, H. S. Mickley, and P. S. Virk, "Disorder distal to modeled stenoses in steady and pulsatile flow.," J. Biomech., vol. 11, no. 10–12, pp. 441–53, Jan. 1978.
- [13] Rupak K. Banerjee, Lloyd H. Back, Martin R. Back, Young I. Cho, "Physiological flow analysis in significant human coronary artery stenoses", Biorheology, 2003.
- [14] P. R. Johnston, D. Kilpatrick, "Modelling human coronary artery blood flow", 1992.
- [15] F. M. White, "Fluid Mechanics", 5th ed. McGraw-Hill, 2003.
- [16] S. N. BARUA, "On secondary flow in stationary curved pipes", 1962.

- [17] W.R. Dean, *"Note on the motion of fluid in a curved pipe"*, Philosophical magazine and Journal of Science, vol. 4, no. 20, pp. 208-223, 1927.
- [18] A. Kalpakli, *"Experimental study of turbulent flows through pipe bends."*, Technical Reports from Royal Institute of Technology KTH Mechanics, April 2012.
- [19] X. Wang, *"computing and applications 1D modeling of blood flow in networks: numerical computing and applications,"* 2015.
- [20] D. Katritsis, L. Kaiktsis, A. Chaniotis et al., *"Wall shear stress: theoretical considerations and methods of measurement"*, Progress in Cardiovascular Diseases, Vol. 49, No. 5, 2007: pp 307-329
- [21] S. Oyre, E. M. Pedersen, S. Ringgaard et al., *"In vivo wall shear stress measured by magnetic resonance velocity mapping in the normal human abdominal aorta."*, Eur J Vasc Endovasc Surg 13, 1997: pp 263-271.
- [22] T. G. Papaioannou, C. Stefanadis, *"Vascular wall shear stress: basic principles and method"*, Hellenic J Cardiol 46, 2005: pp 9-15.
- [23] World Health Organization (WHO), *"The top 10 causes of death"* [Online], available:  
<https://www.who.int/news-room/fact-sheets/detail/the-top-10-causes-of-death>
- [24] [Online] available at: <https://www.hopkinsmedicine.org/health/conditions-and-diseases/anatomy-and-function-of-the-coronary-arteries>
- [25] W. G. Austen et al., *"A reporting system on patients evaluated for coronary artery disease. Report of the Ad Hoc Committee for Grading of Coronary Artery Disease, Council on Cardiovascular Surgery, American Heart Association."*, Circulation, vol. 51, no. 4 Suppl, pp. 5–40, Apr. 1975.
- [26] F. Cademartiri et al. *"Influence of intra-coronary enhancement on diagnostic accuracy with 64-slice CT coronary angiography."*, Eur Radiol, 18(3), pp. 576-83, Mar. 2008.
- [27] P. Consratinides, *"Plaque fissures in human coronary thrombosis"*, Journal of Atherosclerosis Research, 1966.
- [28] S. P. Jackson, W. S. Nesbitt, E. Westein, *"Dynamics of platelet thrombus formation"*, Journal of thrombosis and haemostasis 2009, 7 (Suppl.1), pp. 17-20.
- [29] J. Sheriff, D. Bluestein, G. Girdhar, and J. Jesty, *"High-Shear Stress Sensitizes*

- Platelets to Subsequent Low-Shear Conditions*,” *Ann. Biomed. Eng.*, vol. 38, no. 4, 2010, pp. 1442–1450.
- [30] G. K. Hansson, “*Inflammation, Atherosclerosis and Coronary Artery Disease*”, *N. Engl J Med* 2005;352 pp. 1685-95.
- [31] “*Atherosclerosis*” [Online] available at: <https://www.nhlbi.nih.gov/health-topics/atherosclerosis>
- [32] “*Pathogenesis of Atherosclerosis*” [Online] available at: [http://sphweb.bumc.bu.edu/otlt/MPHModules/PH/PH709\\_Heart/PH709\\_Heart3.html](http://sphweb.bumc.bu.edu/otlt/MPHModules/PH/PH709_Heart/PH709_Heart3.html)
- [33] K. Okrainec, MSc, D. K. Banerjee et al. “*Coronary artery disease in the developing world*”, *Am. Heart J.*, vol. 148, no. 1, pp. 7-15, July 2004
- [34] “*Atherosclerosis.*” [online] Available at: [http://amsacta.unibo.it/3067/116/38\\_aterosclerosis\\_I\\_ed\\_ebook.pdf](http://amsacta.unibo.it/3067/116/38_aterosclerosis_I_ed_ebook.pdf)
- [35] Malek AM, Alper SL, Izumo S., “*Hemodynamic Shear Stress and Its Role in Atherosclerosis*”, *JAMA*, vol. 282(21), pp. 2035–2042, 1999.
- [36] Morbiducci, U. et al., “*Atherosclerosis at arterial bifurcations: evidence for the role of haemodynamics and geometry*”, *Thrombosis and Haemostasis*, vol. 115, no. 03, pp. 484-492, 2016.
- [37] C.G. Caro, J.M. Fitz-Gerald, R.C. Schrother, “*Atheroma and arterial wall shear: observation correlation, and proposal of a shear dependent mass transfer mechanism for atherogenesis*”, *Proc Roy Soc London Ser B*, 1971.
- [38] R.M. Nerem, “*Vascular fluid mechanics, the arterial wall, and atherosclerosis*”, *J Biomech Eng* 1992.
- [39] M. H. Friedman, G. M. Hutchins, C. B. Barger, O. J. Deters, and F. F. Mark, “*Correlation between intimal thickness and fluid shear in human arteries.*”, *Atherosclerosis*, vol. 39, no. 3, pp. 425–36, Jun. 1981.
- [40] A. Cucina, A. V. Sterpetti, G. Pupelis et al., “*Shear stress induces changes in the morphology and cytoskeleton organisation of arterial endothelial cells*”, *Eur J Vascular Surg* 9, 1995: pp 86-92.

- [41] H.C. Stary et al., “A definition of initial, fatty streak, and intermediate lesions of atherosclerosis. A report from the Committee on Vascular Lesions of the Council on Arteriosclerosis, American Heart Association.”, *Circulation*, vol. 89, no.5, pp.2462-78, May 1994.
- [42] “Atherosclerosis.” [Online] available at: <https://en.wikipedia.org/wiki/Atherosclerosis>
- [43] C. G. Valli Guido, “*Bioimmagini*”, Terza ed., Pàtron Editore, Bologna, 2012.
- [44] “Coronary Angiography”, [Online] available at: <http://varglex.napsat.eu/informazioni-sanitarie/langiografia-coronarica>
- [45] S. E. Nissen and P. Yock, “*Intravascular Ultrasound*,” *Circulation*, vol. 103, no. 4, 2001.
- [46] Y.-F. Ma, J.-M. Fam, and B.-C. Zhang, “Critical analysis of the correlation between optical coherence tomography versus intravascular ultrasound and fractional flow reserve in the management of intermediate coronary artery lesion,” *Int. J. Clin. Exp. Med.*, vol. 8, no. 5, pp. 6658–67, 2015.
- [47] B. Ohnesorge and T. Flohr, “Principles of Multi-slice Cardiac CT Imaging,” in *Multi-slice and Dual-source CT in Cardiac Imaging*, Berlin, Heidelberg: Springer Berlin Heidelberg, 2007.
- [48] “Automatic detection of the pulmonary nodules from TC images” [Online] Available: [https://www.researchgate.net/publication/306033192\\_Automatic\\_detection\\_of\\_the\\_pulmonary\\_nodules\\_from\\_CT\\_images](https://www.researchgate.net/publication/306033192_Automatic_detection_of_the_pulmonary_nodules_from_CT_images)
- [49] D. Huang et al., “*Optical Coherence Tomography*”, *Science*, 254(5035), pp. 1178-1181, Nov. 1991.
- [50] M. E. Brezinski et al., “*Imaging of coronary artery microstructure (in vitro) with optical coherence Tomography*”, *Am. Heart J.*, vol. 77, no. 1, pp. 92-93, Jan. 1996
- [51] Y.F. Ma et al., “Critical analysis of the correlation between optical coherence tomography versus intravascular ultrasound and fractional flow reserve in the management of intermediate coronary artery lesion”, *Int J Clin Exp Med*, vol. 8, no. 5: pp. 6658-6667, 2015.
- [52] F. Alfonso et al., “*Diagnosis of spontaneous Coronary Artery Dissection by Optical Coherence Tomography*”, *JACC*, Vol. 59, no. 12, pp. 1075-1079, 2012



- [53] P.A. Tonino et al.; *"FAME Study Investigators. Fractional flow reserve versus angiography for guiding percutaneous coronary intervention."* N Engl J Med, Vol.360, no. 3: pp. 213-24, 2009
- [54] B. De Bruyne et al., *"FAME 2 Trial Investigators. Fractional flow reserve-guided PCI versus medical therapy in stable coronary Disease"*, N Engl J Med, Vol.367, no. 11: pp.991– 1001, 2012.
- [55] S. Valente, A. Mattesini et al., *"Riserva frazionale di flusso: una breve guida pratica all'utilizzo per l'interventista e il punto di vista del cardiologo clinico."*, G. Ital Cardiol, Vol. 18, no. 1: pp. 3S-9S, 2017
- [56] ResearchGate, [Online] Available: [https://www.researchgate.net/figure/Representation-of-the-fractional-flow-reserve-measurement-procedure\\_fig1\\_271534588](https://www.researchgate.net/figure/Representation-of-the-fractional-flow-reserve-measurement-procedure_fig1_271534588)
- [57] P.D. Morris et al, *"Virtual (Computed) Fractional Flow reserve, current challenges and limitations"*, JACC: Cardiovascular Interventions, Vol. 8, No. 8, 2015.
- [58] C.A. Taylor et al, *"Computational Fluid Dynamics applied to cardiac computed tomography for noninvasive quantification of fractional flow reserve."*, JACC, Vol. 61, no. 22, 2013.
- [59] M. Götberg et al., *"Instantaneous Wave-free Ratio versus Fractional Flow Reserve to Guide PCI"*, N Engl J Med. Mar., 2018
- [60] F. Díez-delhoyo et al., *"Coronary physiology assessment in the catheterization laboratory"*, World J Cardiol. 2015 Sep 26; 7(9): pp. 525-538.
- [61] K. Lance Gould et al., *"Anatomic Versus Physiologic Assessment of Coronary Artery Diseases. Role of Coronary Flow Reserve, Fractional Flow Reserve and Positron Emission Tomography imaging in revascularization Decision-Making."*, JACC, Vol. 62, No. 18, October 2013.
- [62] C. Berry et al., *"Fractional Flow Reserve, Coronary Flow Reserve and the Index of Microvascular Resistance in clinical practice."*, RadcliffeCardiology.com, February 2014.
- [63] H. K. Versteeg, W. Malalasekera, *"An introduction to computational fluid dynamics: The finite volume method."*, Second edition, 2007.
- [64] P.D. Morris, A. Narracott et al., *"Computational fluid dynamics modelling in cardiovascular medicine"*, Heart, 0:1-11, 2015

- [65] O. Pironneau, "*FINITE ELEMENT METHODS FOR FLUIDS.*", 1989
- [66] J. (Jean) Donéa and A. Huerta, "*Finite element methods for flow problems.*" Wiley, 2003.
- [67] S. Sankaran, M. E. Moghadam, A. M. Kahn, E. E. Tseng, J. M. Guccione, and A. L. Marsden, "*Patient-specific multiscale modeling of blood flow for coronary artery bypass graft surgery,*" Ann. Biomed. Eng., vol. 40, no. 10, pp. 2228–2242, 2012.
- [68] D. Gallo et al., "*On the Use of In Vivo Measured Flow Rates as Boundary Conditions for Image-Based Hemodynamic Models of the Human Aorta: Implications for Indicators of Abnormal Flow*", Ann Biomed Eng, Vol. 40(3), pp. 729–741, Mar. 2012.
- [69] U. Morbiducci et al., "*Inflow boundary conditions for image-based computational hemodynamics: Impact of idealized versus measured velocity profiles in the human aorta*", J. Biomech., Vol. 41(1), pp. 102–109, Jan. 2013
- [70] M. Schumacher et al., "*Intravascular ultrasound Doppler measurement of blood flow velocity.*", J Neuroimaging, ; Vol. 11(3): pp. 248–52, 2001 Jul.
- [71] D. E. Newby et al., "*Invasive assessment of the coronary circulation: intravascular ultrasound and Doppler*", Br J Clin Pharmacol, vol. 53, no. 6: pp. 561–575, 2002.
- [72] SimVascular, "*Coronary Normal*", [Online] Available: <http://simvascular.github.io/clinicalCase3.html>
- [73] H.J. Kim et al., "*Patient specific modelling of blood flow and pressure in human coronary arteries*", Annals of Biomedical Engineering, Vol. 38, No. 10, October 2010, pp. 3195–3209.
- [74] Z. Duanmu et al., "*A patient-specific lumped-parameter model of coronary circulation*", Scientific Report, 2018.
- [75] A.G. van der Giessen et al., "*The influence of boundary conditions on wall shear stress distribution in patient specific coronary trees*", J. Biomech, Vol. 44, pp. 1089–1095, 2011.
- [76] P.A. Doriot et al., "*In-vivo measurements of wall shear stress in human coronary arteries.*" Coron. Artery Dis. Vol. 11 no. 6, pp. 495–502.
- [77] A.M. Malek et al., "*Hemodynamic Shear Stress and Its Role in Atherosclerosis*", JAMA, Vol. 282, No. 21, December 1, 1999.

- [78] D.N. Ku et al., *"Pulsatile flow and atherosclerosis in the human carotid bifurcation. Positive correlation between plaque location and low oscillating shear stress."*, Arteriosclerosis, vol. 5, no. 3, pp.293-302, 1985 May-Jun.
- [79] U. Morbiducci, *"Indici emodinamici. Descrittori di flusso anomalo."*, Bioengineering of cardiovascular system, 2018.
- [80] G. De Nisco et al., *"The Atheroprotective Nature of Helical Flow in Coronary Arteries"*, Ann Biomed Eng, vol. 47, no 2: pp.425-438, 2019 Feb.
- [81] D. Gallo et al., *"Helical flow in carotid bifurcation as surrogate maker of exposure to disturbed shear."*, J Biomec, vol. 45 (2012), p.p. 2398-2404.
- [82] *"Mesh generation"*, [Online], available:  
<http://simvascular.github.io/docsMeshing.html#intro>
- [83] J.T Marcus et al., *"Flow profiles in the left anterior descending and the right coronary artery assessed by Mr velocity quantification: effects on through-plane and in-plane motion of the heart"*, J Comput Assist Tomogr, vol. 23: pp. 567–576, 1999.